Published in final edited form as:
Nature. 2022 May ; 605(7910): 561–566. doi:10.1038/s41586-022-04699-w.

Structural basis of NPR1 in activating plant immunity

Shivesh Kumar[1,7], **Raul Zavaliev**[2,3,7], **Qinglin Wu**[1,7], **Ye Zhou**[4], **Jie Cheng**[1], **Lucas Dillard**[5], **Jordan Powers**[2,3], **John Withers**[2,3], **Jinshi Zhao**[1], **Ziqiang Guan**[1], **Mario J. Borgnia**[5], **Alberto Bartesaghi**[1,4,6], **Xinnian Dong**[2,3,✉], **Pei Zhou**[1,✉]

[1]Department of Biochemistry, Duke University School of Medicine, Durham, NC, USA.

[2]Department of Biology, Duke University, Durham, NC, USA.

[3]Howard Hughes Medical Institute, Duke University, Durham, NC, USA.

[4]Department of Computer Science, Duke University, Durham, NC, USA.

[5]Genome Integrity and Structural Biology Laboratory, National Institute of Environmental Health Sciences, NIH, Department of Health and Human Services, Research Triangle Park, NC, USA.

[6]Department of Electrical and Computer Engineering, Duke University, Durham, NC, USA.

[7]These authors contributed equally: Shivesh Kumar, Raul Zavaliev, Qinglin Wu.

Abstract

NPR1 is a master regulator of the defence transcriptome induced by the plant immune signal salicylic acid1–4. Despite the important role of NPR1 in plant immunity5–7, understanding of its regulatory mechanisms has been hindered by a lack of structural information. Here we report cryo-electron microscopy and crystal structures of *Arabidopsis* NPR1 and its complex with the transcription factor TGA3. Cryo-electron microscopy analysis reveals that NPR1 is a bird-shaped homodimer comprising a central Broad-complex, Tramtrack and Bric-à-brac (BTB) domain, a BTB and carboxyterminal Kelch helix bundle, four ankyrin repeats and a disordered salicylic-acid-binding domain. Crystal structure analysis reveals a unique zinc-finger motif in BTB for interacting with ankyrin repeats and mediating NPR1 oligomerization. We found that, after stimulation, salicylic-acid-induced folding and docking of the salicylic-acid-binding domain onto ankyrin repeats is required for the transcriptional cofactor activity of NPR1, providing a structural explanation for a direct role of salicylic acid in regulating NPR1-dependent gene expression.

✉**Correspondence and requests for materials** should be addressed to Xinnian Dong or Pei Zhou. xdong@duke.edu; peizhou@biochem.duke.edu.

Author contributions S.K., R.Z., Q.W., J.W., X.D. and P.Z. conceived the project. S.K., Q.W., Y.Z., L.D., J.C., M.J.B., A.B. and P.Z. conducted cryo-EM sample preparation, data collection and processing, and model building. S.K. performed the SAXS study. R.Z. performed in vivo bioassays, including the functional analyses. J.C., Q.W. and P.Z. performed crystallographic studies and data analysis. Q.W. and J.C. performed in vitro biochemical assays. J.Z. and Z.G. performed the MS analysis. J.P. performed the promoter analysis for SA-induced genes. S.K., R.Z., X.D. and P.Z. wrote the manuscript with input from all of the authors.

Competing interests X.D. is a cofounder of Upstream Biotechnology and a scientific advisory board member of Inari Agriculture. The other authors declare no competing interests.

Additional information

Supplementary information The online version contains supplementary material available at https://doi.org/10.1038/s41586-022-04699-w.

Peer review information *Nature* thanks Aardra Kachroo and the other, anonymous, reviewer(s) for their contribution to the peer review of this work.

Reprints and permissions information is available at http://www.nature.com/reprints.

Moreover, our structure of the $TGA3_2–NPR1_2–TGA3_2$ complex, DNA-binding assay and genetic data show that dimeric NPR1 activates transcription by bridging two fatty-acid-bound TGA3 dimers to form an enhanceosome. The stepwise assembly of the NPR1–TGA complex suggests possible hetero-oligomeric complex formation with other transcription factors, revealing how NPR1 reprograms the defence transcriptome.

As a positive regulator that is required for systemic acquired resistance mediated by salicylic acid (SA) in plants, the *NONEXPRESSOR OF PATHOGENESIS-RELATED GENES 1* (*NPR1*) gene was identified more than two decades ago in *Arabidopsis*[1–4]. Since then, the central role of NPR1 in controlling plant responses against a broad spectrum of pathogens has been firmly established[5–7]. Notably, overexpression of *Arabidopsis* NPR1 in a wide range of plant species, including many crops, has been shown to enhance disease resistance against a variety of pathogens and stresses[8], indicating that the protein has intrinsic properties underlying its broad protective functions. Despite its importance in plant immunity and potential agricultural application, the molecular architecture of NPR1 has remained unclear, hindering mechanistic understanding of its regulation and function.

The cryo-EM structure of apo NPR1

As the first step towards structural analysis of NPR1, we expressed and purified the full-length *Arabidopsis* NPR1 using insect cells. Interestingly, this ~66 kDa protein eluted between standards of 440 kDa and 158 kDa in size-exclusion chromatography (Extended Data Fig. 1a, b). Treatment of NPR1 with the cross-linking agent BS3 yielded predominantly a dimer band on the SDS–polyacrylamide gel electrophoresis (SDS–PAGE) gel (Extended Data Fig. 1c). As NPR1 was purified in the presence of 2 mM dithiothreitol (DTT) without SA, our result indicates that dimeric NPR1 represents its reduced apo form.

The structure of the NPR1 dimer was determined using single-particle cryo-electron microscopy (cryo-EM) at a resolution of 3.8 Å (Extended Data Fig. 1d–h and Extended Data Table 1). The overall shape of the protein resembles a gliding bird (Fig. 1a). At the centre of the dimer lies the core BTB domain[9], which consists of a three-stranded β-sheet (B1–B3) flanked by five helices (A1–A5; Fig. 1b). Similar to other homodimeric BTB domains[9], the NPR1 BTB domain contains an additional dimerization helix at the N terminus (α0; Fig. 1a, b); however, it lacks a domain-swapped β-strand preceding the dimerization helix in these proteins[9]. C terminally to the BTB domain, NPR1 contains a unique four-helix bundle that shares the helical pair repeat pattern with the BTB and carboxyterminal Kelch (BACK) domain[10,11], but is much shorter than BACK (4 versus 8 helices) and is therefore named the BACK helix bundle (BHB). The first pair of helices in the BHB superimpose very well with the CUL3-binding box (3-box) in the ubiquitin ligase adaptor speckle-type POZ protein (SPOP)[12] (Fig. 1c). Similar to SPOP[13], the removal of the BHB does not abolish the CUL3A interaction (Extended Data Fig. 2a).

After the BHB is an extended linker loop connecting the BHB to ankyrin repeats (ANKs) (Fig. 1b, d). NPR1 contains three well-defined ANKs[14–16] and a non-canonical fourth ANK with two α-helices linked by a 16-residue loop (Fig. 1d). The last three ANKs are connected by characteristic β-hairpins, whereas the first two ANKs are joined by a loop (Fig. 1d).

These four ANKs pack against the central BTB/BHB through the first helices of individual ANKs, leaving the second ANK helices solvent exposed. A characteristic feature of ANKs is the presence of conserved histidine residues bridging neighbouring repeats[15]. Similarly, His300 of ANK2 and His334 of ANK3 form extensive hydrogen bonds with residues from the neighbouring ANK3 and ANK4 units (Fig. 1d). Genetic mutations of these histidine residues (*nim1–2*, H300Y; *npr1–1*, H334Y) cause a loss of *PATHOGENESIS-RELATED* (*PR*) gene expression and profound defects in systemic acquired resistance[1,3,5,6].

Beyond the ANKs, no density can be observed for the C-terminal putative SA-binding domain (SBD)[17], consistent with it being disordered as revealed by small-angle X-ray scattering (SAXS) measurements (Extended Data Fig. 2b).

NPR1 contains a zinc finger

As EM densities in some functionally important regions of NPR1 did not provide sufficient resolution for confident model building, we crystallized NPR1(ΔSBD) (Thr39–Asp410), which diffracted to 3.06 Å (Extended Data Table 2). X-ray fluorescence scanning revealed the presence of Zn^{2+} ions in the protein crystal, but not in the buffer (Extended Data Fig. 3a). Accordingly, analysis of the crystal structure revealed a distinct C_2HC zinc finger within a functionally important cysteine cluster that is conserved in NPR1 and its homologues[6,18], but is absent in mammalian BTB domains (Extended Data Fig. 3b). The Zn^{2+} ion is coordinated by Cys150, Cys155, His157 and Cys160 in a consensus sequence of **C**-X-**D**-$X_{2/3}$-**C**-X-**H**-X_2-**C** located within the A3-A4 loop of the BTB domain (Fig. 2a, b), where bold letters and Xs indicate conserved and non-conserved residues, respectively. Consistent with previous functional studies[6,18,19], we found that npr1(C150A), npr1(C150Y; npr1–2), npr1(C155A), npr1(C155Y; npr1–35) and npr1(C160A) are defective in their interaction with the TGA3 transcription factor and transcriptional activity when transiently expressed in *Nicotiana benthamiana* (Fig. 2c, d). Notably, the npr1(H157A) mutation did not affect the activation of the *PR1* promoter (Fig. 2d), suggesting that npr1(H157A) may partially retain its ability to form a zinc finger, similar to the reported zinc-finger mutant of the HIV-1 nucleocapsid protein[20].

As part of its role in maintaining the structural integrity, the zinc finger bridges the BTB domain to ANK4 through a network of polar interactions (Fig. 2a (inset)). The carboxylate group of Asp152, the most conserved residue within the zinc finger besides the zinc-coordinating residues, forms two hydrogen bonds with side chains of Lys370 and Gln371 of ANK4. The zinc-finger–ANK4 interaction is also ‘zip-locked’ by backbone hydrogen bonds involving Glu149 and Ala151 from the zinc finger, and Lys370, Thr373 and Ala375 from ANK4. As Lys370 is located at the last turn of the ANK helix, the Ala151–Lys370 backbone hydrogen bond is fortified by the helix dipole effect[21]. Supporting the functional importance of the zinc finger–ANK4 interaction, simultaneously mutating Asp152 to a basic residue (D152R) and disrupting the backbone hydrogen bond of Ala151 (A151P) in npr1(A151P/D152R) abolished the TGA3 interaction and *PR1* induction (Fig. 2c, d).

Moreover, the formation of the zinc finger, with side chains of Cys155 and His157 pointing inwards to coordinate Zn^{2+}, pivots Cys156 directly into solvent (Fig. 2a (inset)). Our previous study has shown that NPR1 in the quiescent state forms a homo-oligomer that is held together by intermolecular disulphide bonds, whereas, in response to SA induction, NPR1 is released through the activity of thioredoxins to trigger systemic acquired resistance[22]. Notably, we found that, in the crystal structure, the protein lattice is formed by head-to-head stacking of two NPR1 dimers, and the pair of Cys156 residues from each NPR1 dimer are juxtaposed against their counterparts in the tetramer (Fig. 2e). Similar to our previous study of the NPR1 BTB domain[22], we found that hydrogen peroxide treatment of the NPR1 BTB–BHB domain (Thr39–Lys262) readily yielded dimer, trimer and tetramer bands on the non-reducing SDS–PAGE (Fig. 2f). The NPR1 C156A mutation strongly reduced dimer formation and eliminated oligomer bands (trimer and tetramer), supporting Cys156 as a redox sensor. Within the NPR1 dimer at the monomer–monomer interface lie two Cys82 residues also in proximity (Fig. 2e), and the C82A mutation reduced the formation of trimer and tetramer bands (Fig. 2f), consistent with our previous genetic data[18]. By contrast, a C212V/C216A/C223L triple-mutant behaved similarly to the WT protein, suggesting that these remaining non-zinc-chelating cysteine residues in the BTB–BHB do not contribute to redox-mediated NPR1 oligomerization in vitro.

SA induces docking of the SBD onto ANK3/4

Even though NPR1 contains all of the SA-binding residues in the SA receptor NPR4, and binds to SA with a sub-micromolar dissociation constant (K_d) value[17,23,24], its binding capacity is low, suggesting that only a small percentage of the recombinant SBD has the ability to bind to SA in vitro[17], possibly due to the absence of a chaperone. To mitigate this problem, we refolded full-length NPR1 in the presence of 0.2 mM SA and subjected it to extensive purification before preparing cryo-EM samples.

Analysis of cryo-EM 2D class averages of the NPR1–SA complex revealed similar features of the BTB–BHB–ANKs architecture as those in apo NPR1, confirming that NPR1 was properly refolded (Fig. 1e, Extended Data Fig. 4 and Extended Data Table 1). Notably, in the SA-bound state, additional densities were readily visible near the C termini of the ANKs of the NPR1 dimer (Fig. 1e), suggesting that SA induced the folding of the SBD.

The reconstructed 3D density map revealed that the SBD largely consists of helices (Fig. 1f), although the limited resolution in this region prevented detailed structural modelling. Aided by the recently reported structure of the NPR4 SA-binding core with a SA-containing four-helix bundle[17], we modelled the SBD using SWISS-MODEL[25] and docked the structure onto the extra density of the NPR1–SA complex. In the structural model (Fig. 1f), the strongest density was observed in the α2-helix of the SBD (Fig. 1f, g). Although densities of the three ‘standing’ helices (α1, α3 and α4) are visible near the ANKs, they fade rapidly as these helices extend away from the ANKs (Fig. 1f). A well-defined hydrophobic interface is formed between Ile450 of the α2-helix and Phe507 and Phe508 at the conjunction of the α3–α4 helices of the SBD and Leu346, Leu393 and Ile397 of ANK3 and ANK4 (Fig. 1g). Notably, Leu346 is one of the three residues mutated in *npr1(sim3)* that block NPR1 SUMOylation and transcriptional activity[26]. Similarly, the F507S and F508S mutations in *Arabidopsis* NPR1 or the corresponding residues (F505S and F506S) in tobacco (*N. benthamiana*) NPR1 abolish its binding to the transcription repressor NIMIN1/2 (refs. [27,28]). Effects caused by these mutations suggest that the observed interaction between SBD and ANKs might modulate the function of NPR1.

To test whether perturbation of the SBD–ANK interaction can affect NPR1 function, we mutated hydrophobic ANK residues at the interface (L346D, L393D and I397D; Fig. 1g) and found that all three mutations diminished SA-induced *PR1* gene expression (Fig. 1h), even though two mutants (L346D and L393D) retained the interaction with TGA3 (Fig. 1i). We next tested whether locking the SBD–ANK interaction could boost the NPR1 function by introducing two cysteine residues, one in the SBD (R506C) and one in the ANKs (Q400C/E401L), to cross-link the SBD–ANK docking conformation through a disulphide bond. We found that the resulting mutant (Q400C/E401L/R506C) significantly elevated gene expression (Fig. 1j) without changing the interaction with TGA3 (Fig. 1k). Taken together, our results indicate that the SBD–ANK-docking conformation is required for NPR1 in promoting defence gene transcription.

NPR1 bridges two TGA3 dimers through ANK1

To elucidate how SA-induced NPR1 activates TGA transcriptional activity, we determined the cryo-EM structure of NPR1 in complex with TGA3 in the presence of DNA carrying the TGA *cis*-element *as-1* (LS7)[29]. Supporting the complex formation, extra densities are readily visible near ANK1 of NPR1 at one or both sides of the NPR1 dimer (Fig. 3a, b). Given the dimeric nature of NPR1, we hypothesize that the double-sided complex reflects the final assembly (Fig. 3a), whereas the single-sided complex reflects an assembly intermediate (Fig. 3b). Density maps of both complexes were reconstructed, each with an overall resolution of 3.6 Å (Extended Data Fig. 5 and Extended Data Table 1).

Surprisingly, EM analysis revealed that each extra density represents a dimer of the TGA3 C-terminal domain, which, to the best of our knowledge, has not been reported to form a stable dimer. Owing to its role of engaging NPR1, we named it the NPR1-interacting domain (NID) (Fig. 3a–c). The TGA3 NID contains five prominent long helices (α1, α2, α6, α7 and α8) and three short helices (α3, α4 and α5; Fig. 3c). Four long helices (α1, α2, α6 and α7) form an arched layer, whereas three short helices (α3, α4 and α5) zig-zag across the layer and support the C-terminal helix (α8), which tilts away from the arched layer. The NID dimer is formed through extensive interactions between the three short helices (α3, α4 and α5) and between the tilted α8 helix in one monomer and the α6–α7 helices in the other monomer (Fig. 3c). Unexpectedly, a palmitic acid was found inside the NID, an observation corroborated by the 1.5 Å resolution crystal structure and mass spectrometry (MS) analysis (Fig. 3d, Extended Data Fig. 6 and Extended Data Table 2). This observation further implicates lipid metabolism in regulating plant immunity[30,31].

NPR1–TGA3 binding is mediated by elaborate interactions (Fig. 3e). Surface-exposed hydrophobic residues from ANK1 of NPR1, such as Leu281 and Leu284, project onto a hydrophobic concave surface of one TGA3 subunit formed by the α5–α6 loop (Pro264 and Thr266) and α7–α8 loop (Thr351), whereas numerous hydrogen bonds and salt bridges are observed between ANK1 residues (Lys272, Ser276, Asp277, Asp278, Glu280, Glu288 and His290) and TGA3 NID residues from the α5–α6 loop (Glu263), α6 helix (Asp267), α8 helix (Thr352, Arg353 and Arg357). Corroborating these observations, mutating interfacial residues in NPR1, such as L281D and L284D, abolished the NPR1–TGA3 interaction (Fig. 3f) and SA-induced *PR1* gene expression (Fig. 3g).

In the NPR1 complex with TGA3, weak density of the SBD can also be visualized (Fig. 3a, b). Despite the limited resolution, which prevents model building, it is evident that the SBD has no direct contact with TGA3. Notably, in the single-sided $NPR1_2$–$TGA3_2$ assembly intermediate, the unengaged NPR1 subunit has much weaker densities in its ANKs and SBD than the subunit engaged in TGA3 binding (Fig. 3b), suggesting that the stability of ANKs may be dynamically regulated. Moreover, no density was observed for DNA or the basic-leucine zipper (bZIP) region of TGA3, suggesting that the DNA-binding domain is separated from the NID by a flexible linker.

The NPR1 dimer is required in plant immunity

The structure of the $TGA3_2$–$NPR1_2$–$TGA3_2$ complex, with the dimeric NPR1 engaging two TGA3 dimers, suggests that NPR1 may serve as a transcription cofactor by bridging two transcription factor complexes in an enhanceosome. Consistent with this hypothesis, the *as-1* element is significantly enriched in the promoters of top 100 SA-induced genes[32], and 77 contain at least two *as-1* elements that are frequently separated by <50 bp (Extended Data Fig. 7a–c). On the basis of this information, we conducted the electrophoresis mobility shift assay (EMSA) using the *PR1* gene promoter containing two *as-1* elements (LS5 and LS7)[29], which are both required for NPR1-mediated transcription in a reporter assay[33]. The addition of TGA3 yielded two upshifted bands of the promoter DNA, corresponding to single and double occupancy of the *as-1* elements, but not the negative-control DNA with both *as-1* elements replaced by adenosines (Fig. 4a). Although NPR1 itself did not bind to DNA, it completely supershifted the TGA3 double-occupancy band and depleted the single-occupancy band. Moreover, mutating either of the two *as-1* elements in the DNA blocked the NPR1-mediated supershift band (Extended Data Fig. 7d). These results support our hypothesis that the NPR1 dimer activates TGA transcription factor activity by bridging two DNA-bound TGA complexes.

To test our hypothesis genetically, we designed a dimerization-deficient *npr1(dim)* mutant by introducing L49D/F53D/V56D/V83K mutations into the α0 and A1 helices of the NPR1 BTB dimer interface (Fig. 4b), following a similar strategy to disrupt the dimerization of the SPOP BTB domain[12]. The npr1(dim) mutant not only failed to self-interact (Fig. 4c), but also eluted off the size-exclusion column at a later volume than WT NPR1 (Extended Data Fig. 8a). A low-resolution cryo-EM map of npr1(dim) revealed a single-wing shape, confirming that the mutations disrupted dimerization without affecting the overall protein architecture (Extended Data Fig. 8b).

Before testing the transcriptional activity of npr1(dim), we evaluated its ability to form a quiescent homo-oligomer, which has been shown to prevent NPR1 nuclear translocation[18,22]. We found that npr1(dim) was deficient in oligomer formation and had increased nuclear accumulation (Fig. 4d, e), similar to the npr1(C82A) mutant[18]. However, in contrast to *npr1(C82A)*, which has constitutive *PR1* gene expression, npr1(dim) was unable to induce the *PR1* promoter when transiently expressed in *N. benthamiana* (Fig. 4f), probably because it is unable to cross-link the TGA complexes (Fig. 4a). Similarly, in stable transgenic lines, npr1(dim)–GFP failed to activate *PR1*, *WRKY18*, *WRKY38* and *WRKY62* (Fig. 4g), all of which have at least two *as-1* elements in their promoters (Extended Data Fig. 7b). As a consequence, in contrast to WT plants, the *npr1(dim)-GFP* plants were compromised in SA-induced defence against *Pseudomonas syringae* pv. maculicola ES4326, whereas the npr1(C82A) mutant, which is able to dimerize (Extended Data Fig. 8a), conferred constitutive resistance (Fig. 4h). These results establish the NPR1 homodimer as the functional unit that is required not only for oligomer formation in the quiescent state, but also for NPR1 function in inducing defence gene expression and resistance against pathogen challenge.

This study establishes a structural framework for explaining data from over two decades of NPR1 studies (Fig. 4i). The lack of a direct contact between SBD and TGA suggests that the SBD–ANK-docking conformation may enable post-translational modification, such as SUMOylation, that is required for NPR1 activity[26], and/or facilitate the recruitment of an unknown transcription regulator. The need for investigating new regulatory factors is reinforced by our unexpected observation of a palmitic acid within the TGA3 NID. The structural elucidation of the $TGA3_2$–$NPR1_2$–$TGA3_2$ complex and its assembly intermediate raises the possibility that NPR1 reprograms the defence transcriptome in response to a wide range of biotic and abiotic stresses through the engagement of not only TGA homodimers, but also heterologous transcription activators, suppressors and lipid metabolites in an enhanceosome complex (Fig. 4i).

Online content

Any methods, additional references, Nature Research reporting summaries, source data, extended data, supplementary information, acknowledgements, peer review information; details of author contributions and competing interests; and statements of data and code availability are available at https://doi.org/10.1038/s41586-022-04699-w.

Methods

Cryo-EM studies of apo NPR1, NPR1–SA and the npr1(dim) mutant

Cloning, expression and purification using insect cells.—Full-length *Arabidopsis thaliana NPR1* and the corresponding *npr1(dim)* mutant (L49D/F53D/V56D/V83K) were cloned into the pFASTBac1 vector as a His_{10}–GST–NPR1–Strep fusion protein containing a PreScission protease site after GST. Baculovirus was generated and amplified according to the manufacturer’s protocol (Thermo Fisher Scientific) using Sf9 cells (Expression Systems). For protein expression, *Trichoplusia ni* (High Five) cells were cultured in the ESF 921 insect cell culture medium (Expression Systems) at 27 °C; the suspension cell culture was infected with a high-titre baculovirus stock and collected after 50 h by centrifugation at 200*g* for 5 min. Cell pellets were resuspended and lysed by sonication in the purification buffer (25 mM HEPES pH 7.5 and 150 mM NaCl) and supplemented with protease inhibitors (15 μM leupeptin, 1 μM pepstatin A, 2 μM E-64, 0.1 μM aprotinin, 1 mM phenylmethylsulphonyl fluoride) and DNase I. After centrifugation at 15,000 rpm and 4 °C for 15 min, the fusion protein was purified using the Strep-Tactin Superflow Plus resin (Qiagen). After PreScission protease cleavage to remove the His_{10}–GST tag, the WT protein or the npr1(dim) mutant were further purified by passing it through the Talon resin (Takara Bio) and eluted from the column in the presence of 10–15 mM imidazole in the lysis buffer, whereas the His_{10}–GST tag was retained on the cobalt column.

WT NPR1 was concentrated and further purified by size-exclusion chromatography using the Superose 6 increase 10/300 GL column (Cytiva) pre-equilibrated with the purification buffer containing 2 mM DTT. Peak fractions were concentrated and cross-linked using 2 mM BS3 (Thermo Fisher Scientific) at room temperature for 30 min, and the cross-linked sample was further purified by size-exclusion chromatography (Superose 6 increase 10/300 GL; Cytiva) for cryo-EM grid preparation.

The npr1(dim) mutant used for cryo-EM grid preparation was purified using identical procedures as the WT NPR1.

The SA-bound NPR1 was obtained by refolding NPR1 in the presence of SA. In brief, purified NPR1–Strep was concentrated and dialysed against 8 M urea followed by dialysis in the refolding buffer containing 25 mM HEPES (pH 7.5), 150 mM NaCl, 2 mM DTT and 0.2 mM SA. The refolded sample was purified by size-exclusion chromatography using the Superose 6 increase 10/300 GL column (Cytiva) pre-equilibrated with the refolding buffer. The peak fraction was then concentrated and cross-linked with 2 mM BS3 as described above; the cross-linked sample was repurified by size-exclusion chromatography (Superose 6 increase 10/300 GL; Cytiva) for cryo-EM grid preparation.

Cryo-EM sample preparation and data collection.—The cryo-EM grids containing NPR1 were prepared using the Leica EM GP Automatic Plunge Freezer at 10 °C and 95% humidity. The UltrAuFoil R1.2/1.3 300-mesh grids were glow-discharged using the Tergeo-EM plasma cleaner (Pie Scientific). A 3 μl sample of BS3 cross-linked NPR1 (~0.6 mg ml^{-1}) was applied to the grids and blotted for 2–3 s with Whatman No. 1 filter paper (Whatman International) to remove excess sample and plunge-frozen into liquid ethane cooled by liquid nitrogen. A total of 1,638 micrograph stacks were collected with SerialEM[35] on a Talos Arctica microscope at 200 kV equipped with a K2 Summit direct electron detector (Gatan), at a nominal magnification of 45,000× and defocus values from −2.5 μm to −0.8 μm, yielding a pixel resolution of 0.9317 Å px^{-1}. Each stack was exposed for 8.4 s with an exposing time of 0.14 s per frame, resulting in 60 frames per stack. The total dose was approximately 60 e^{-} $Å^{-2}$ for each stack.

The cryo-EM grids containing NPR1–SA were prepared similarly to that of NPR1. A total of 9,486 micrograph stacks were collected with SerialEM[35] on a Titan Krios microscope (Thermo Fisher Scientific) at 300 kV equipped with a K3 direct electron detector (Gatan), at a nominal magnification of 64,000× and defocus values from −2.5 μm to −0.8 μm, yielding a pixel resolution of 0.5325 Å px^{-1}. Each stack was exposed for 8.069 s with an exposing time of 0.134 s per frame, resulting in 60 frames per stack. The total dose was approximately 60 e^{-} Å^{-2} for each stack.

The cryo-EM grids containing the npr1(dim) mutant were prepared similarly except that C-flat R1.2/1.3 300-mesh grids (Protochips) coated with gold were used. A total of 3,500 movies were recorded with a defocus range from −2.0 μm to −0.8 μm on the Talos Arctica electron microscope (Thermo Fisher Scientific) at 200 kV equipped with a K3 Summit direct electron detector (Gatan) at a nominal magnification of 45,000× (0.88 Å px^{-1}) using SerialEM[35]. Each stack was exposed for 2.716 s with an exposing time of 0.045 s per frame. The total dose was approximately 55 e^{-} Å^{-2} distributed over 60 frames.

Cryo-EM data processing and model building.—For cryo-EM data analysis of apo NPR1, movie alignment was performed in RELION[36] and the parameters of the contrast transfer function (CTF) were determined on the motion corrected sum of frames using CTFFIND4.1 (ref. [37]). Micrographs (1,391) were selected on the basis of the CTF fit resolution using a cut-off of 4.5 Å. A total of 615,647 NPR1 particles were boxed out using template-free particle picking. Two consecutive rounds of 2D classification were performed to clean the extracted particles. A total of 125,604 clean particles were used for further processing. The processing flow chart is shown in Extended Data Fig. 1d. In brief, a consensus reconstruction obtained with cryoSPARC[38] using all of the clean particles resulted in a map at ~6 Å resolution. Four ab initio 3D references were generated and processed for multi-reference 3D classification using heterogeneous refinement. A subset of 38,117 particles showing the best structural features was selected and processed for homogeneous refinement without applying symmetry. Non-uniform refinement using C_2 symmetry yielded a reconstruction with an overall resolution of 4.2 Å. The resolution improved to 4.0 Å after one round of local refinement. At this point, another subset of 37,588 particles identified from the previous heterogeneous refinement were added and processed for a new round of non-uniform refinement using C_2 symmetry, yielding a 3.8 Å reconstruction. A focus refinement extended the resolution of the centre domain of the dimer to 3.6 Å. The de novo model building for apo NPR1 was conducted using COOT[39]. The region containing the cysteine cluster (Glu149–Cys160) was initially built as polyalanines due to the limited local resolution. This region was rebuilt on the basis of the knowledge of a zinc finger from crystal structure analysis of NPR1. Structure refinement was performed using PHENIX[40] in real space with secondary and geometry restraints.

The NPR1–SA dataset was processed in a similar manner to that described above. A total of 5,424 micrographs were selected on the basis of the CTF fit resolution with a cut-off value of 4.5 Å. Around 5.6 million particles were used for 2D classification after curating the template-free blob picking results. After three rounds of cleaning with 2D classification, 120,893 particles were selected and imported back to RELION[36] for refinement. The apo NPR1 map and mask were used as the 3D reference for the consensus refinement with C_2 symmetry focusing on the NPR1 dimer core domain, which resulted in a 4.0 Å map. 3D classification without alignment was conducted (no mask or symmetry applied). One good class containing 117,529 particles was selected and processed for local refinement with a shape mask yielding an overall resolution of 3.9 Å. A summary of the processing flow chart is shown in Extended Data Fig. 4.

For the npr1(dim) dataset, movie alignment and the CTF estimation were conducted using cryoSPARC[38]. A total of 2,377 micrographs were selected based on the CTF fit resolution cut-off of 4 Å. Manually picked particles were used as input for Topaz particle picking[41]. Rounds of 2D classification were performed to isolate good classes. Two ab initio models were generated and processed for heterogeneous refinement. A subset of 18,795 particles showing better structural features was selected for homogeneous refinement.

Cloning, overexpression and purification of the NPR1 SBD for biological SAXS.—The *Arabidopsis* NPR1 SBD (Pro412–Arg593) was cloned into the pFASTBac1 vector as a His_{10}–GST–NPR1–Strep fusion protein containing a PreScission protease site following GST. The baculovirus generation, protein expression and purification followed similar procedures as described for NPR1. The protein was concentrated to 1 mg ml^{-1} in a buffer containing 25 mM HEPES (pH 7.5), 150 mM NaCl and 2 mM DTT for biological SAXS measurements at beamline 12-ID-B of the Advanced Photon Source (APS).

Cryo-EM studies of the NPR1–TGA3 complex

Expression and purification of *Arabidopsis* NPR1 and TGA3 using *Escherichia coli*.—Full-length *Arabidopsis NPR1* was cloned into the pTrcHis vector (Thermo Fisher Scientific) as a His_{10}–MBP–fusion protein containing a PreScission protease site following MBP and a C-terminal Strep tag (Strep3) with the last Lys residue of the Strep tag mutated to Arg. Transformed BL21(DE3) *E. coli* cells were grown in Luria–Bertani (LB) medium at 37 °C to an optical density at 600 nm (OD_{600}) of 0.5, induced with 0.1 mM IPTG, 0.1 mM $ZnSO_4$ and 0.2 mM SA at 18 °C overnight. The purification of the *E. coli*-expressed NPR1 was performed as described above for the insect-cell-expressed NPR1, except that the purification buffer contained 0.2 mM SA.

Arabidopsis TGA3 (Asn87–Thr384) was cloned into the pTrcHis vector (Thermo Fisher Scientific) as a His_{10}–MBP fusion protein containing a PreScission protease site following MBP and a C-terminal tandem Flag–HA tag. Transformed BL21(DE3) *E. coli* cells were grown in LB medium at 37 °C to an OD_{600} of 0.5 and induced with 0.1 mM IPTG at 18 °C overnight. The purification was performed as described above for NPR1.

NPR1–TGA3–LS7-DNA cryo-EM sample preparation.—The purified NPR1–Strep3 (20 μM), TGA3–Flag–HA (48 μM) and the LS7 DNA containing a palindromic TGA-binding site (underlined in 5′-CACTATT TTAC<u>TGACGTCA</u>TAGATGTGGCG-3′, 57.6 μM) were mixed and incubated at 4 °C for 30 min. The protein–DNA complex was cross-linked with 1.5 mM BS3 (Thermo Fisher Scientific) at room temperature for 30 min and quenched with 50 mM Tris (pH 8.0). The protein–DNA mixture was further purified using a Strep-Tactin column (Qiagen) and size-exclusion chromatography (Superose 6 increase 10/300 GL, Cytiva) in a buffer containing 25 mM HEPES (pH 7.5), 150 mM NaCl, 2 mM DTT and 0.2 mM SA.

Cryo-EM sample preparation and data collection.—Cryo-EM grids containing the NPR1–TGA3–LS7-DNA complex were prepared using the Leica EM GP2 Automatic Plunge Freezer at 4 °C and 85% humidity. The UltrAuFoil R1.2/1.3 300-mesh grids

(Quantifoil) were glow-discharged using the PELCO easiGlow Glow Discharge Cleaning System (Ted Pella). A 3 μl sample of NPR1–TGA3–LS7-DNA (~1.3 mg ml^{-1}) was applied to the grid, incubated for 60 s in the chamber and blotted for 2.4 s with Whatman No. 1 filter paper (Whatman International) to remove excess sample, and then plunge-frozen into liquid ethane cooled by liquid nitrogen. A total of 9,442 micrograph stacks were collected with SerialEM[35] on a Titan Krios microscope (Thermo Fisher Scientific) at 300 kV equipped with a K3 direct electron detector (Gatan), at a nominal magnification of 81,000× and defocus values from −2.0 μm to −1.0 μm, yielding a resolution of 1.066 Å px^{-1}. Each stack was exposed for 8.3 s with an exposing time of 0.138 s per frame, resulting in 60 frames per stack. The total dose was approximately 60 e^{-} $Å^{-2}$ per stack.

Cryo-EM data processing and model building.—For cryo-EM data analysis of $TGA3_2$–$NPR1_2$–$TGA3_2$, movie alignment and the CTF estimation were conducted using cryoSPARC[38]. A total of 8,988 micrographs were selected based on the CTF fit resolution using a cut-off value of 4.0 Å. A total of around 14 million particles were boxed out using the NPR1 as the template. Multiple rounds of 2D classification and selection were performed to clean the extracted particles. A total of around 881,000 clean particles were used for further processing. The processing flow chart is shown in Extended Data Fig. 5 and summarized below. In brief, three classes with clear TGA3 densities on both sides of NPR1 were selected for ab initio reconstruction and homogeneous refinement with C_2 symmetry of the $TGA3_2$–$NPR1_2$–$TGA3_2$ complex. A total of 165,208 particles that were selected from the clean set of particles were processed for 3D classification/heterogeneous refinement using apo NPR1 and the low-resolution $TGA3_2$–$NPR1_2$–$TGA3_2$ maps as the template. A subset of 94,144 particles featuring the $TGA3_2$–$NPR1_2$–$TGA3_2$ complex were processed for homogeneous refinement with C_2 symmetry. Non-uniform refinement was then performed using C_2 symmetry, yielding a reconstruction with an overall resolution of 3.6 Å. Focused refinements of $NPR1_2$ (central region) and two $TGA3_2$ (left and right regions) extended local resolutions to 3.5 Å and 4.0 Å, respectively. A composite map was generated using PHENIX[40] for model building.

Similarly, 536,200 particles were selected for reconstruction of the $NPR1_2$–$TGA3_2$ complex. After ab initio reconstruction and 3D classification/heterogeneous refinement, 287,150 particles were selected for homogenous and non-uniform refinement, yielding an overall resolution of 3.6 Å. Focused refinement of $NPR1_2$ (excluding the weak ANK region), $TGA3_2$ and the weak ANK region extended local resolutions to 3.4 Å, 3.6 Å and 4.0 Å, respectively.

The de novo model building was conducted using COOT[39]. Structure refinement was performed using PHENIX[40] in real space with secondary structure and geometry restraints.

X-ray crystallography studies of NPR1(ΔSBD) and the TGA3 NID

Arabidopsis NPR1(ΔSBD) (Thr39–Asp410) was cloned into the pTrcHis vector (Thermo Fisher Scientific) as a His_{10}-MBP fusion protein containing a PreScission protease site following MBP and a C-terminal Strep tag. Expression and purification of NPR1(ΔSBD) was performed using similar procedures to those described above for *E. coli*-expressed

NPR1, except that the size-exclusion chromatography buffer contained 20 mM HEPES (pH 7.5), 150 mM NaCl and 1 mM TCEP. Protein crystals were grown using the sitting-drop vapour diffusion method at 20 °C. Each drop was prepared by mixing 1 μl of the protein solution at 6 mg ml^{-1} with 1 μl of the reservoir solution containing 0.1 M HEPES (pH 7.5), 19% PEG 3350, 0.25 M tri-sodium citrate. Diffraction-quality protein crystals were collected after 1 week and cryoprotected with the reservoir solution containing 25% glycerol.

The *Arabidopsis* TGA3 NID (Ala160–Thr384) was cloned into the pTrcHis vector (Thermo Fisher Scientific) as a His_{10}–MBP fusion protein containing a PreScission protease site following MBP and a C-terminal tandem Flag–HA tag. The purification procedure was performed similarly to that of *Arabidopsis* TGA3 (Asn87–Thr384) except that the size-exclusion chromatography buffer contained 20 mM HEPES (pH 7.5), 150 mM NaCl and 1 mM TCEP. Protein crystals were grown using the sitting-drop vapour diffusion method at 20 °C. Each drop contained 1 μl of the protein solution mixed with 1 μl of the reservoir solution (0.1 M sodium acetate at pH 5.0, 20% (v/v) MPD). Diffraction quality protein crystals were collected after 1 week and cryoprotected with the reservoir solution also containing 25% glycerol.

X-ray fluorescence and diffraction datasets of NPR1(ΔSBD) were collected at the Northeastern Collaborative Access Team (NECAT) 24-ID-C beamline at the Advanced Photon Source at the Argonne National Laboratory. The X-ray diffraction data were processed using XDS[42]. The phase information was obtained by molecular replacement with the PHASER module in the PHENIX suite[40] using the cryo-EM coordinates of apo NPR1 and the TGA3 subunit in the $NPR1_2$–$TGA3_2$ complex as the search model for NPR1(ΔSBD) and the TGA3 NID, respectively. Iterative model building and refinement were performed using COOT[39] and PHENIX[40]. For NPR1(ΔSBD), the final model has 95.13% residues in the favoured region, 4.87% in the allowed region and 0.0% in the outlier region of the Ramachandran plot. For the TGA3 NID, the final model has 99.01% residues in the favoured region, 0.99% residues in the allowed region and 0.0% in the outlier region of the Ramachandran plot.

Lipid extraction from the TGA3 NID and LC–ESI/MS analysis

The fatty acid was extracted from the purified TGA3 NID protein using the two-phase Bligh–Dyer method[43]. The extract was analysed using normal-phase liquid chromatography–electrospray ionization/MS (LC–ESI/MS) in negative mode using an Agilent 1200 Quaternary LC system coupled to a high-resolution TripleTOF5600 mass spectrometer (Sciex) as previously described[44]. Data acquisition and analysis were performed using the Analyst TF1.5 software (Sciex).

In vitro NPR1 oxidation

WT NPR1 BTB/BHB (Thr39–Lys262) and the npr1(C156A), npr1(C82A) and npr1(C212V/C216A/C223L) mutants were cloned into the pTrcHis vector (Thermo Fisher Scientific) as His_{10}–MBP fusion proteins with a PreScission protease site following MBP and a C-terminal Strep tag. The proteins were expressed and purified similarly to the NPR1(ΔSBD) as described above. The NPR1 BTB/BHB WT and mutant proteins at a concentration of 25 μM were incubated with 1 mM hydrogen peroxide in a buffer containing 125 mM HEPES and 150 mM NaCl at pH 8.0 at room temperature for 45 min. The oxidized samples were incubated with 50 mM iodoacetamide for 5 min, mixed with 4× SDS loading dye and analysed using SDS–PAGE in the absence of any reducing reagent.

Promoter analysis for *as-1* elements

For the promoter analysis, the scanMotifGenomeWide.pl function in HOMER (v.4.11) was initially used to generate a bed file containing all *as-1* elements in the *Arabidopsis* genome. Moreover, using R (v.4.1.1) and the Araport 11 GTF, bed files for the 3,000 bp upstream regions of the top 100 induced and of all the uninduced genes in response to 8 h of treatment by the SA analogue benzothiadiazole[32] were generated. The window function in bedtools (v.2.30.0) with a window of 0 bp was used to intersect both promoter and *as-1* element bed files to generate bed files containing all *as-1* elements within the 3,000 bp upstream regions of the top 100 SA-induced genes and uninduced genes. The number of *as-1* elements in each promoter was counted and the *as-1*-element count distribution of the top 100 SA-induced genes was compared to the distribution of uninduced genes using a χ^2 test. The promoters of the top 100 SA-induced genes were further analysed for multiple *as-1* elements and subset into groups containing 0, 1, 2 or more *as-1* elements. The distances between *as-1* elements in the same promoter were computed and plotted as a histogram binned every 50 bp using R (v.4.1.1).

Gel EMSA

The *npr1(dim)* mutant (L49D/F53D/V56D/V83K) was cloned into the pTrcHis vector (Thermo Fisher Scientific) as a His$_{10}$–MBP fusion protein containing a PreScission protease site following MBP and a C-terminal Strep tag, and was expressed and purified similarly to the WT NPR1 protein. Purified TGA3 (Asn87–Thr384) at a concentration of 0.6 μM and WT NPR1 or the npr1(dim) mutant at a concentration of 8 μM were used in the EMSA with the 6-fluorescein (6-FAM)-labelled oligonucleotide probes (200 nM) containing the LS5 and LS7 *as-1 cis*-elements of the SA-responsive *PR1* gene promoter (LS5/LS7, 6-FAM-C-gggCTATGACGTAAGTAAAATAGTGACGTAGAGAggg) or DNA sequences with the two *as-1* regions replaced with adenosines (LS5$^-$/LS7$^-$, 6-FAM-C-gggCTAAAAAAAAAGTAAAATAGAAAAAAAAAAGAggg), with the LS7 *as-1* element replaced with adenosines (LS5/LS7$^-$, 6-FAM-C-gggCTATGACGTAAGTAAAATAGAAAAAAAAAAGAggg) or with the LS5 *as-1* element replaced with adenosines (LS5$^-$/LS7, 6-FAM-C-gggCTAAAAAAAAAGTAAAATAGTGACGTAGAGAggg) as well as their complementary oligonucleotides (Integrated DNA Technologies). The uppercase bases indicate the LS5/LS7 sequence; the lowercase bases indicate overhangs outside the LS5/LS7 sequence; and bases replaced with adenosines are indicated with As in the small capital font. Pairs of complementary DNA strands were annealed before the binding reaction. For each binding reaction, the desired protein combination was mixed with the target DNA probe together with 30 ng μl^{-1} of poly(dI-dC) (non-specific competitor, Thermo Fisher Scientific) in a binding buffer containing 20 mM HEPES (pH 8.0), 300 mM NaCl, 10% glycerol, 1 mM DTT and 0.2 mM SA. The mixture was incubated at 4 °C for 30 min and then run on a 3.8% native polyacrylamide gel in the TB buffer (100 mM Tris-borate pH 8.3, 10% glycerol). After electrophoresis, the gel was scanned with the Typhoon FLA 7000 imager (GE Healthcare).

Plant material and transformation

A. thaliana mutants, and transgenic plants are all in the Col-0 ecotype background. *Arabidopsis* mutant *npr1–2* (ref. [6]), and transgenic lines expressing NPR1–GFP in the *npr1–2* background and npr1(C82A)–GFP in the *npr1–1* background were described previously[18,45]. Transgenic *Arabidopsis* expressing npr1(dim)–GFP in the *npr1–2* background was generated and two independent lines homozygous for the transgene were used. Seeds were stratified at 4 °C for 3 days before sowing and plants were grown under 12 h–12 h light–dark cycles at 22 °C. *N. benthamiana* plants were grown under the same conditions.

The coding sequences of WT *AtNPR1* (AT1G64280) and *AtTGA3* (AT1G22070), as well *AtNPR1* mutants generated with the QuikChange II site-directed mutagenesis kit (Agilent), were subcloned into the pDONR207 gateway donor vector and confirmed by sequencing. The *npr1* mutants were designed based on the structural information. The SBD–ANK cross-linked mutant npr1(Q400C/E401L/R506C) was designed based on the proximity and geometry of Gln400 and Arg506 side chains in the docked conformation of the NPR1 SBD onto ANKs. The E401L mutation was introduced to compensate for the loss of the Glu401–Arg506 hydrogen bond and avoid burial of a charged residue at the protein interface. The obtained entry vectors carrying WT or mutated genes were recombined into the plant binary vectors pK7FWG2, pLN462 and pSITE-4NB to generate C-terminal eGFP, HA and mRFP fusion proteins, respectively. The *pPR1:DUAL-LUC* reporter was described previously[46].

For plant transformations, the *Agrobacterium tumefaciens* strain GV3101 was transformed with plant binary vectors carrying the indicated transgenes. For stable expression in *Arabidopsis*, a floral dipping method was used[47]. For transient expression in *N. benthamiana*, the *Agrobacterium* carrying the indicated construct was cultured overnight at 28 °C in LB broth medium supplemented with appropriate antibiotics: spectinomycin (100 $\mu g\ ml^{-1}$), kanamycin (50 $\mu g\ ml^{-1}$), gentamycin (50 $\mu g\ ml^{-1}$) and rifampicin (25 $\mu g\ ml^{-1}$). The obtained culture was re-inoculated at 1:10 into fresh growth medium with antibiotics and grown for another 4 h. Cells were then centrifuged at 1,600*g* for 10 min, and inoculum was prepared by resuspending cells to an OD_{600} of 1 in double-distilled water containing 200 μM acetosyringone (Sigma-Aldrich). The co-expression assays were performed with a 1:1 mixture of *Agrobacteria* inoculums. The inoculum was pressure-infiltrated into *N. benthamiana* leaves at the abaxial side using 1 ml syringe without the needle.

In planta gene expression analysis

Expression of the defence genes *PR1*, *WRKY18*, *WRKY38* and *WRKY62* in transgenic *Arabidopsis* was performed by quantitative PCR (qPCR). Total RNA was extracted from fresh leaf tissue with Trizol reagent (Sigma-Aldrich). cDNA was synthetized using the SuperScript III cDNA Synthesis kit (Thermo Fisher Scientific). qPCR was performed using the FastStart Universal SYBR Green Master Kit (Roche) using the Mastercycler ep realplex

(Eppendorf) system. A list of the gene-specific primers used for qPCR is provided in Supplementary Table 1.

The *PR1* promoter activity was tested using dual-luciferase (DUAL-LUC) reporter assay as described previously[46]. The *pPR1:DUAL-LUC* reporter was transiently co-expressed in *N. benthamiana* together with HA-fused NPR1 or its mutants as effectors. The free HA effector was used as a negative control. Plants were treated with 2 mM SA for 24–30 h at 1 day after inoculation. At 2 days after inoculation, leaf discs were collected, ground in liquid nitrogen and lysed with the passive lysis buffer (PLB) of the Dual-Luciferase Reporter Assay System (Promega, E1910). Lysate was centrifuged at 12,000*g* for 1 min, and 10 μl was taken for measuring firefly LUC (F-LUC) and *Renilla* LUC (R-LUC) activities according to the manufacturer's instructions using the Victor3 plate reader (PerkinElmer). At 25 °C, substrates for F-LUC and R-LUC were added using the automatic injector and, after 3 s shaking and 3 s delay, the signals were captured for 3 s and recorded as counts per second. To obtain the *PR1* promoter activity, the ratio of F-LUC over the R-LUC activities was calculated for each effector.

Protein analysis

Recombinant protein analysis, co-immunoprecipitation and cell-free oligomerization were performed using total protein extracts from the transient expression assay in *N. benthamiana* as described previously[46]. Interaction analysis of NPR1–HA with TGA3–mRFP or NPR1–GFP (self-interaction), was performed in vivo by transiently co-expressing the two proteins in *N. benthamiana* followed by treatment with water (mock) or 1 mM SA for 5 h. Total protein was extracted and used for co-immunoprecipitation with anti-RFP or anti-HA beads, respectively. In the NPR1–HA/TGA3–mRFP interaction experiments the npr1–1–HA was used as a negative control. Interaction between GST–NPR1 and Myc–CUL3A was performed by co-expression in *E. coli* as described[46]. For western blotting under reducing conditions, the SDS sample buffer was added to the protein extracts from a 4× stock solution supplemented with 50 mM DTT and 715 mM β-mercaptoethanol. For western blotting under non-reducing conditions, a DDT- and β-mercaptoethanol-free SDS sample buffer was used. The blots were probed with anti-GFP (Clontech, 632381, 1:5,000), anti-HA (BioLegend, 901513, 1:1,000), anti-RFP (ChromoTek, 6G6, 1:5,000), anti-cMyc (Santa Cruz, SC-40, 9E10, 1:1,000) or anti-GST-HRP (GE Healthcare, RPN1236V, 1:10,000) primary antibodies. Secondary anti-mouse-HRP antibodies (Abcam, Ab97040) were used at 1:20,000.

NPR1 oligomerization assay in plant extract

For the cell-free oligomerization assay, total proteins were extracted with lysis buffer (50 mM Tris-HCl pH 7.5, 150 mM NaCl, 0.2% Triton X-100, 0.2% Nonidet P-40, 5% glycerol) supplemented with 1 mM PMSF, 100 μM MG132, EDTA-free protease inhibitor cocktail and 14.3 mM β-mercaptoethanol. The obtained lysate was diluted 10-fold with the lysis buffer supplemented with 1 mM PMSF, 100 μM MG132 and EDTA-free protease inhibitor cocktail. The samples were incubated in the dark at 4 °C for 0, 1, 2 and 3 h time periods before SDS–PAGE analysis under reducing or non-reducing conditions.

Pathogen infection

For soil-grown *Arabidopsis* plants, SA treatment was carried out with spray at 1 mM concentration 24 h before gene expression analysis or bacterial infection. For bacterial infection, *P. syringae* pv. maculicola ES4326 (*Psm* ES4326) was grown for 2 days on solid King's B medium supplemented with 100 μg ml^{-1} streptomycin. An inoculum was prepared by resuspending cells in 10 mM $MgSO_4$ to obtain an OD_{600} of 0.001. Bacteria were pressure-infiltrated into mature leaves of three-week old *Arabidopsis* plants and bacterial growth was assessed at 3 days after inoculation by collecting leaf disks from eight infected plants per treatment/genotype, ground in 10 mM $MgSO_4$, and plated at sequential dilutions on King's B medium plates supplemented with 100 μg ml^{-1} streptomycin. At 2 days after inoculation, the bacterial colonies were scored.

Confocal imaging

Confocal fluorescence microscopy was performed using the Zeiss 880 airyscan inverted confocal microscope with a ×40/1.2 NA water correction objective. eGFP was excited with a 488 nm argon laser and emission was collected with a 505–530 nm bandpass filter. NPR1–GFP or npr1(dim)–GFP localization was tested in leaf epidermal cells of *N. benthamiana* after transient expression. To determine nucleocytoplasmic partitioning, the fluorescence intensities from the entire cell (total) and from nuclei were quantified from 15–20 randomly sampled unsaturated confocal images (512 × 512 px, 225 × 225 μm) using an automated image analysis algorithm implemented in the ImageJ software[48] as previously described[49]. The obtained intensity values were used to calculate the ratio of nuclear signal over total signal in Microsoft Excel.

Statistics and reproducibility

Data plotting and statistical tests were performed in GraphPad Prism 8. Statistical parameters such as mean ± s.d. and 95% confidence intervals are indicated in the figure legends. In the graphs, asterisks and lowercase letters indicate statistical significance tested either by Student's *t*-tests (two groups) or ANOVA (multiple groups) at a significance threshold of $P < 0.05$. The number of biological replicates is indicated for all the data in figure captions. In the figures, the individual datasets (Figs. 1h, j, 2d, 3g and 4e–h) and images (Figs. 1i, k, 2c, f, 3f and 4a, c–e) are representative of at least two experimental repeats.

Reporting summary

Further information on research design is available in the Nature Research Reporting Summary linked to this paper.

Data availability

The data supporting the findings of this study are available within the paper and its Supplementary Information. The cryo-EM structures of the apo NPR1, $NPR1_2$–$TGA3_2$ and $TGA3_2$–$NPR1_2$–$TGA3_2$, and X-ray crystal structures of the NPR1(ΔSBD) and TGA3 NID have been deposited at the PDB (www.pdb.org) under accession codes 7MK2, 7TAD, 7TAC, 7MK3 and 7TAE, respectively. The cryo-EM density maps of apo NPR1, NPR1–

SA, NPR1_2–TGA3_2 and TGA3_2–NPR1_2–TGA3_2 have been deposited to the Electron Microscopy Data Bank under accession codes EMD-23884, EMD-23885, EMD-25771 and EMD-25769, respectively. There are no restrictions on data availability. Source data are provided with this paper.

Extended Data

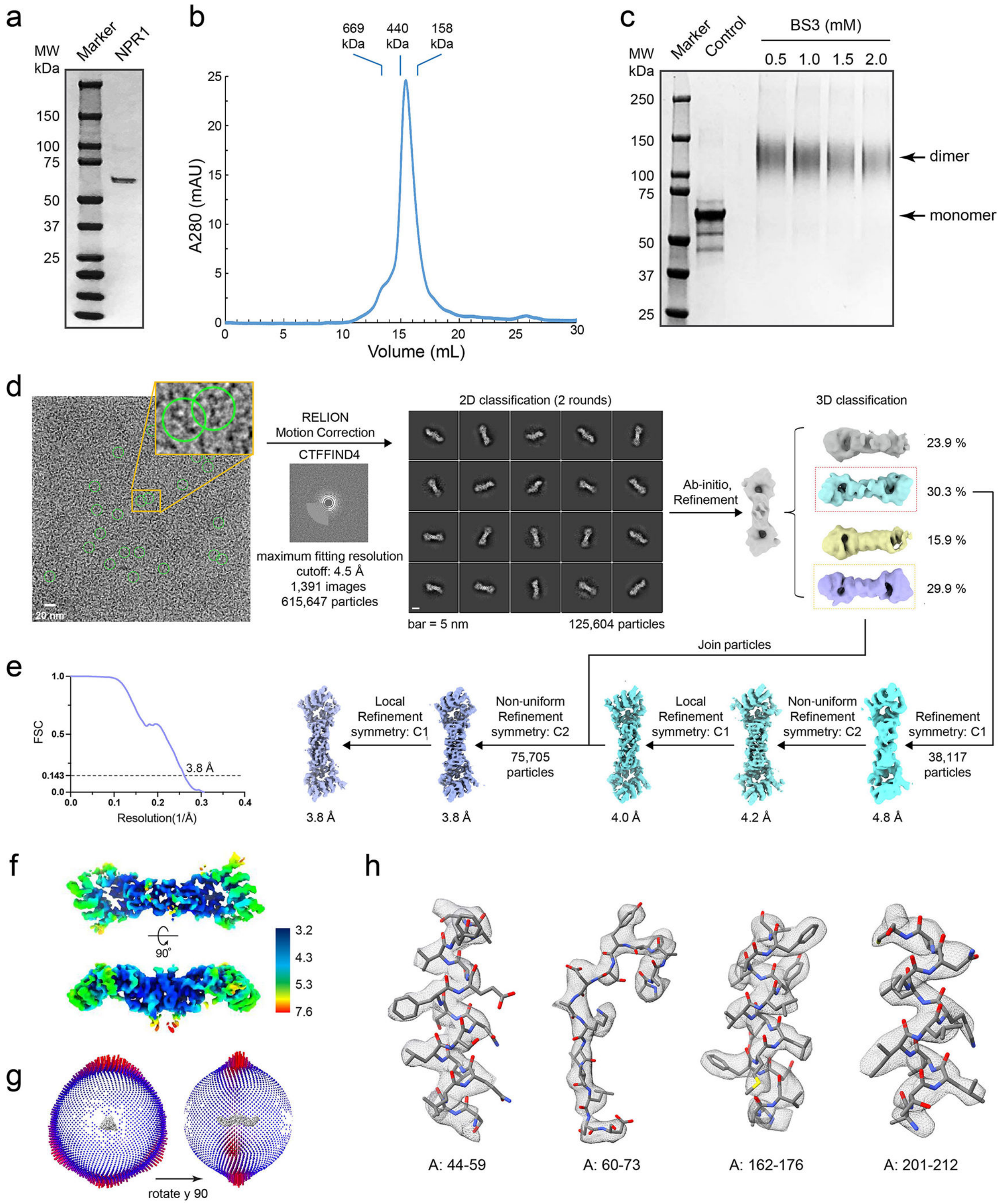

Extended Data Fig. 1 |. Biochemical characterization and cryo-EM reconstruction of apo NPR1.

a, SDS–PAGE gel of purified NPR1. **b**, Size-exclusion chromatography shows that NPR1 elutes between molecular weight markers of 440 kDa and 158 kDa on a Superose 6 Increase 10/300 GL column. **c**, Crosslinking of NPR1 by BS3 at varying concentrations reveals a dominant dimer band. **d**, Flowchart of the reconstruction. Details are described in Methods. Green circles highlight representative NPR1 particles on the micrograph with the enlarged view in the inset. **e**, The global Fourier Shell Correlation (FSC) curve. **f**, Local resolution map. **g**, Euler angle distribution of the particles. **h**, Representative regions of the EM density map. Images in **a** and **c** are representative of 3 and 2 biological replicates, respectively.

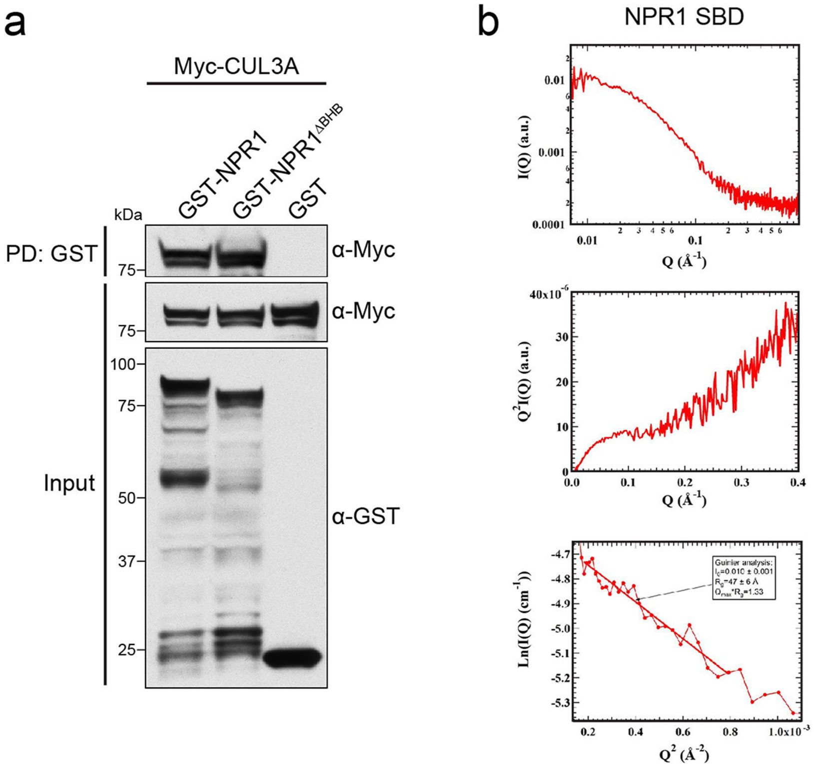

Extended Data Fig. 2 |. Biochemical characterization of the NPR1 BHB and SBD domains.

a, Interaction of Myc-tagged CUL3A (Myc-CUL3) with free GST, or GST-fused WT NPR1 (GST–NPR1), or NPR1$^{\Delta BHB}$ deletion mutant (deletion of E200-L258; GST–NPR1$^{\Delta BHB}$) in *E. coli*. The proteins were co-expressed in *E. coli* and total lysate was used for pull-down with glutathione affinity resin. Images are representative of 2 biological replicates. **b**, Solution small angle X-ray scattering (SAXS) data for the *Arabidopsis* apo NPR1 SBD purified from insect cells at a concentration of 1 mg ml^{-1}. The SAXS scattering curve, the Kratky plot, and the Guinier analysis are shown in the top, middle, and bottom panels, respectively. The non-bell shape of the Kratky plot indicates the protein is unfolded and exhibits a random-coil behaviour. The Guinier analysis yields a large radius of gyration (Rg) value of 47 Å for the NPR1 SBD (~20 kDa) in comparison with folded lysozyme (14.3 kDa; Rg = ~16 Å) and Bovine serum albumin (66 kDa; Rg = ~30 Å), indicating a disordered conformation.

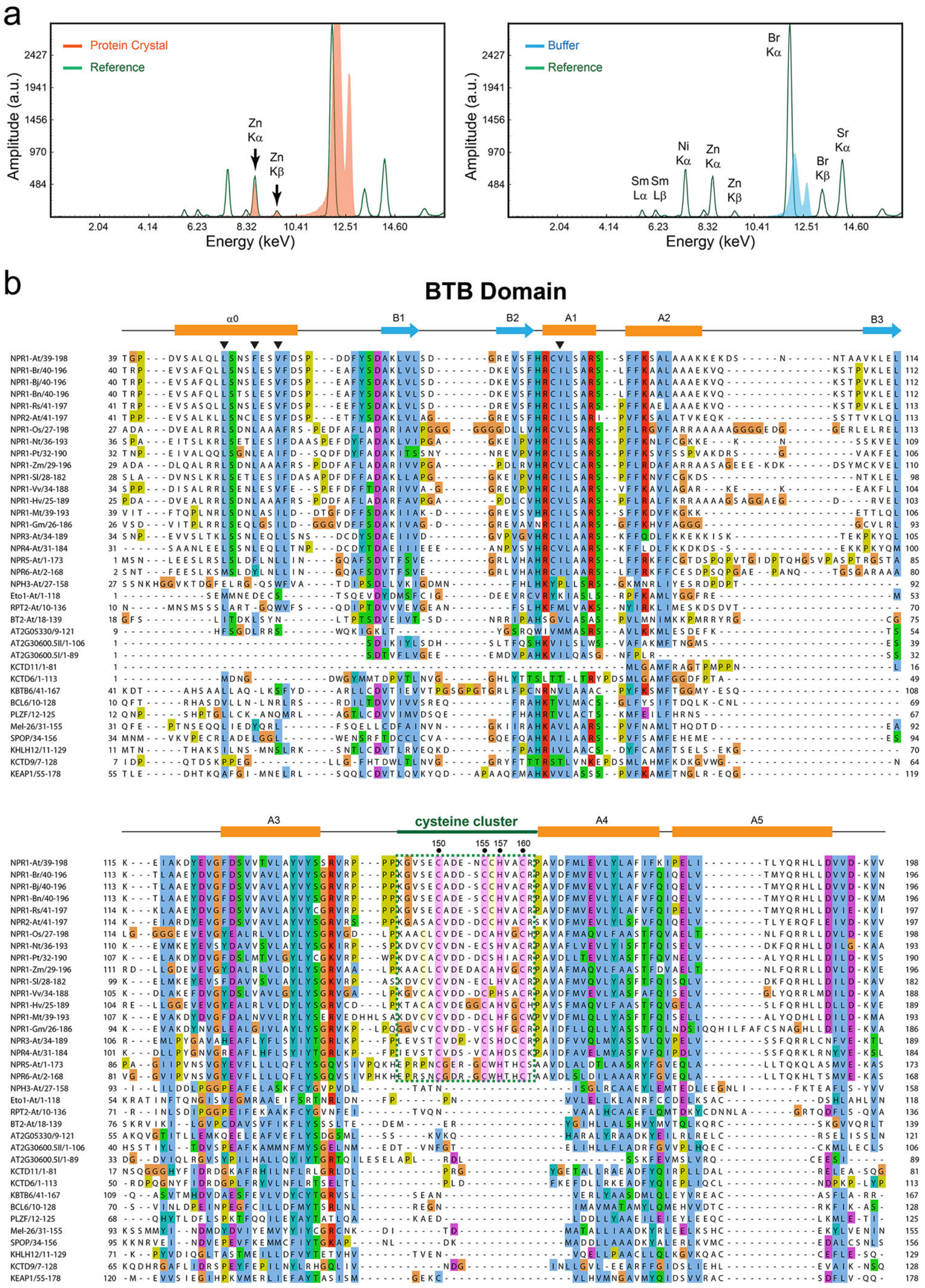

Extended Data Fig. 3 |. NPR1 harbours a unique zinc finger.

a, X-ray fluorescence scanning data revealed the presence of Zn^{2+} in NPR1(ΔSBD) crystals. Scanning results for the NPR1 protein crystal and buffers are shown in the left and right panels, respectively. **b**, Sequence alignment of BTB domains. Conserved cysteine and histidine residues in a unique cysteine cluster preserved in NPR proteins are highlighted in pink. Dots indicate residues participating in zinc coordination, and triangles denote residues mutated in npr1(dim). Listed plant species include: *Arabidopsis thaliana* (*At*), *Brassica rapa* (*Br*), *Brassica juncea* (*Bj*), *Brassica napus* (*Bn*),*Raphanus sativus* (*Rs*), *Oryza sativa* (*Os*), *Nicotiana tabacum* (*Nt*), *Populus trichocarpa* (*Pt*), *Zea mays* (*Zm*), *Solanum lycopersicum* (*Sl*), *Vitis vinifera* (*Vv*), *Hordeum vulgare* (*Hv*), *Medicago truncatula* (*Mt*), and *Glycine max* (*Gm*).

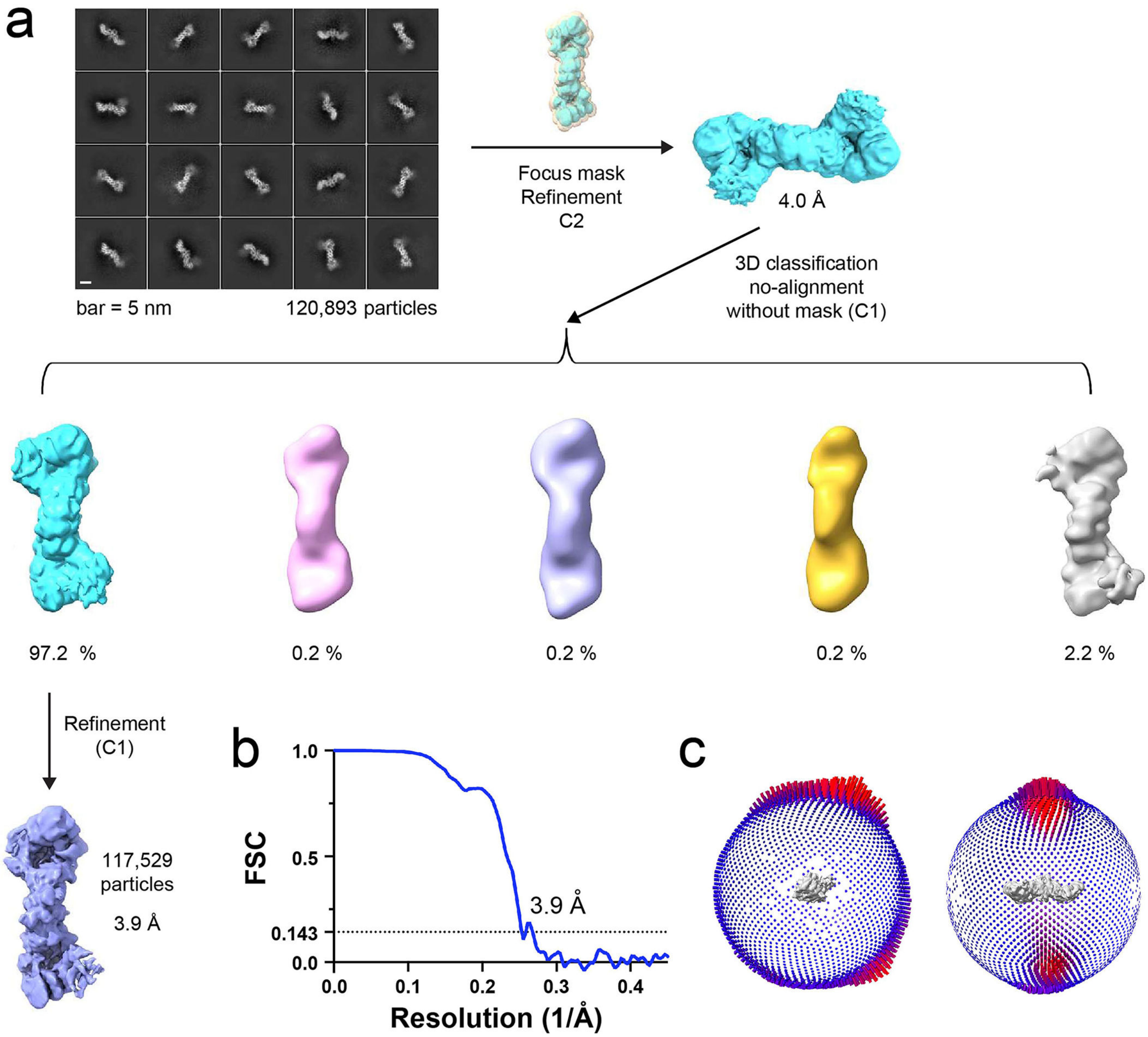

Extended Data Fig. 4 |. Cryo-EM reconstruction of the NPR1-SA complex.

Details of the flowchart are described in Methods. **a**, Flowchart of the reconstruction. **b**, Global Fourier Shell Correlation (FSC) curve. **c**, Euler angle distribution of the particles.

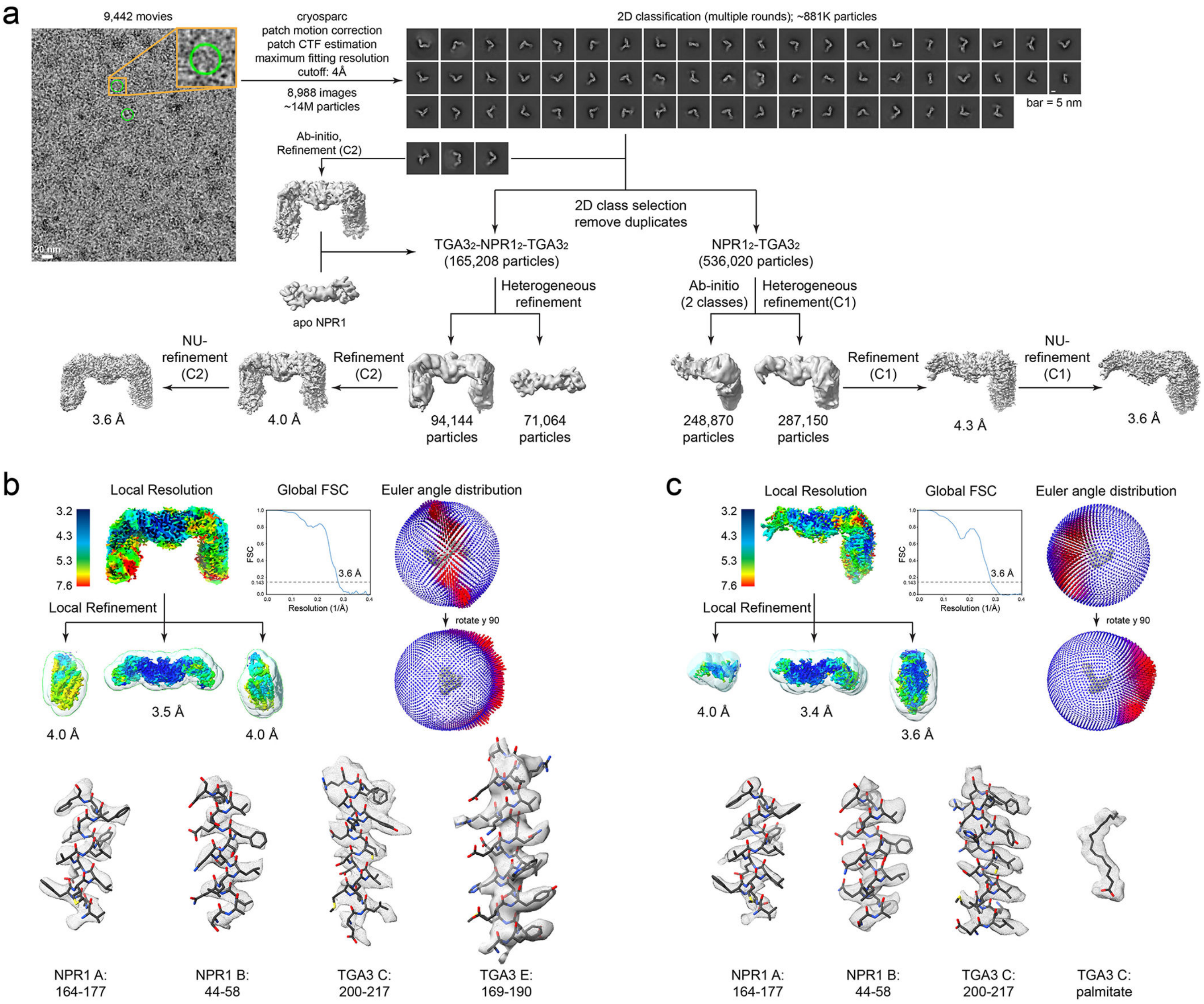

Extended Data Fig. 5 |. Cryo-EM reconstruction of the NPR1–TGA3 complex.

a, Flowchart of the reconstruction. **b**, Local resolution, global Fourier Shell Correlation (FSC) curve, Euler angle distribution of the particles, and representative regions of the EM density map of the TGA3$_2$–NPR1$_2$–TGA3$_2$ complex. **c**, Local resolution, global FSC curve, Euler angle distribution of the particles, and representative regions of the EM density map of the NPR1$_2$–TGA3$_2$ complex.

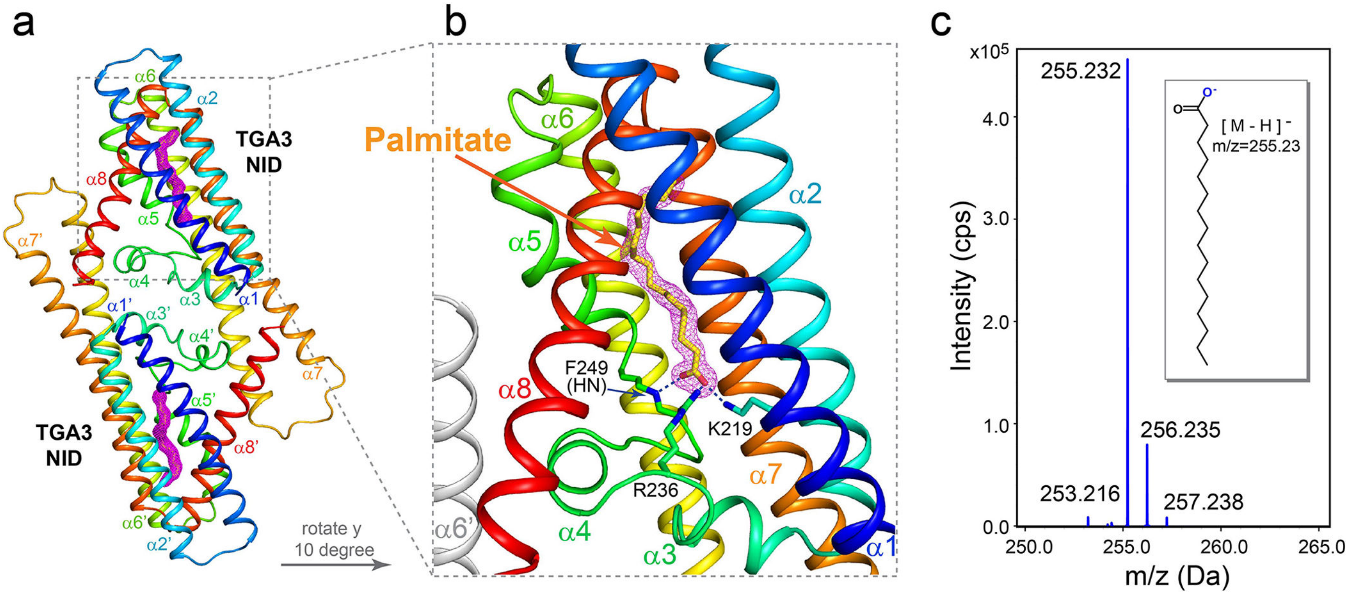

Extended Data Fig. 6 |. Crystallographic and mass spectrometry characterization of the TGA3 NID–palmitate complex.

a, Crystal structure of the TGA3 NID dimer. The two TGA3-NID molecules are shown in the rainbow colour, with N-terminus coloured in blue and C-terminus coloured in red. **b**, A zoomed-in view of the location of the palmitate. Polar interactions with the carboxylate group of the palmitates are indicated with dashed lines. For clarity, only one TGA3 molecule is coloured in rainbow, and the other molecule is coloured in grey. Purple meshes in panels **a**, **b** represent 2mFo-DFc omit map of the palmitate plotted at the 1.0 σ level. **c**, Mass spectrometry analysis of the fatty acid extracted from the protein sample, verifying the fatty acid as the palmitic acid (C16:0).

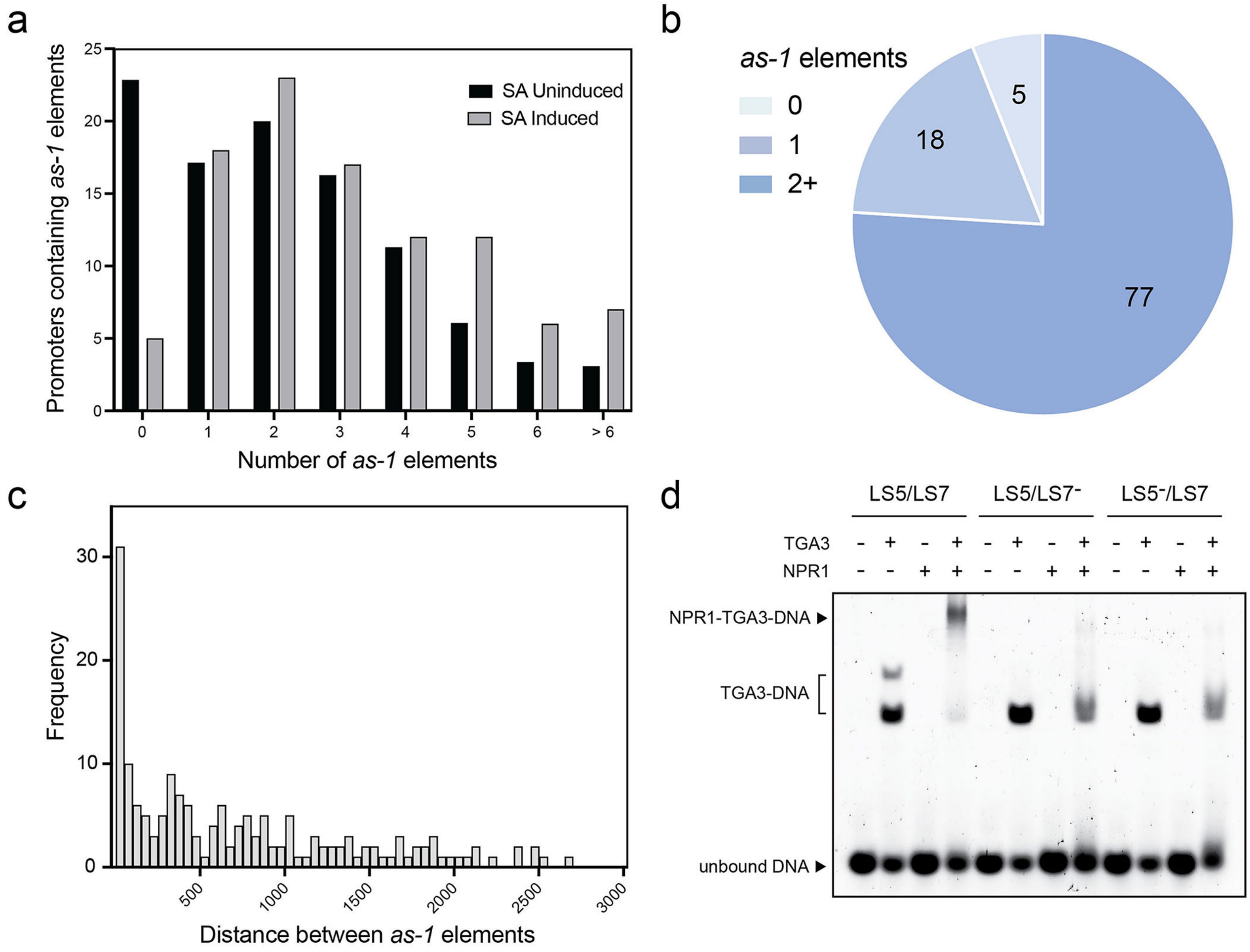

Extended Data Fig. 7 |. The *as-1* elements in SA-induced gene promoters.

a, Distribution of *as-1* element in the promoters (3 kb) of SA-uninduced genes compared to the promoters (3 kb) of top 100 SA-induced genes[32]. A statistically significant difference of *as-1* element distribution was seen in the promoters of the top 100 SA-induced genes compared to the promoters of SA-uninduced genes (p-value < 0.001). **b**, Promoter analysis for *as-1* elements of the top 100 SA-induced genes after 8 h treatment. **c**, Frequency plot of distances between *as-1* elements from the promoters of the top 100 SA-induced genes. **d**, Electrophoresis mobility shift assay of NPR1 and TGA3 using 6-fluorescein-labelled DNA spanning the LS5-to-LS7 region of the *PR1* promoter containing two *as-1* elements (LS5/LS7) or a single *as-1* element in the LS5 region (LS5/LS7$^-$) or in the LS7 region (LS5$^-$/LS7). **d** is a representative image of 3 biological replicates.

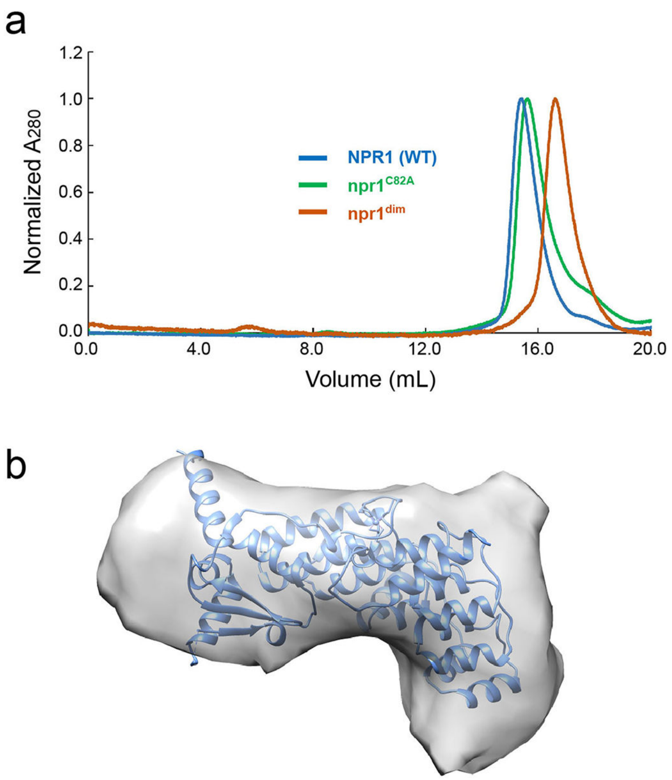

Extended Data Fig. 8 |. Characterization of the npr1(dim) mutant.

a, Elution profiles of the WT NPR1, npr1(C82A), and npr1(dim) samples on a Superose 6 Increase 10/300 GL column. **b**, A low resolution cryo-EM map of npr1(dim) reveals the expected shape of a monomeric NPR1. The monomeric model of NPR1 has been fitted into the EM density and displayed in the cartoon representation.

Extended Data Table 1 |

Cryo-EM data collection, refinement, and validation statistics of the *Arabidopsis* full-length NPR1, NPR1-SA, TGA3_2-NPR1_2-TGA3_2, and NPR1_2-TGA3_2 complexes

	NPR1 (EMDB-23884) (PDB 7MK2)	**NPR1-SA complex (EMDB-23885)**	**TGA3_2-NPR1_2-TGA3_2 complex (EMDB-25769) (PDB: 7TAC)**	**NPR1_2-TGA3_2 complex (EMDB-25771) (PDB 7TAD)**
Data collection and processing				
Magnification	45,000	64,000	81,000	81,000
Voltage (kV)	200	300	300	300
Electron exposure (e−/Å^2)	60	60	60	60
Defocus range (pm)	[−2.25, −1.25]	[−2.0, −0.5]	[−2.0, −1.0]	[−2.0, −1.0]
Pixel size (Å)	0.9317	1.065	1.066	1.066
Symmetry imposed	C2	C1	C2	C1
Initial particle images (no.)	615,647	5.7 M	14 M	14 M

	NPR1 (EMDB-23884) (PDB 7MK2)	**NPR1-SA complex (EMDB-23885)**	**TGA3$_2$-NPR1$_2$-TGA3$_2$ complex (EMDB-25769) (PDB: 7TAC)**	**NPR1$_2$-TGA3$_2$ complex (EMDB-25771) (PDB 7TAD)**
Final particle images (no.)	75,705	120,893	94,144	287,150
Map resolution (Å)	3.8	3.9	3.6	3.6
FSC threshold	0.143	0.143	0.143	0.143
Map resolution range (Å)	3.2–4.3	3.4–6.0	3.2–7.6	3.2–7.6
Refinement				
Initial model used (PDB code)	N/A		N/A	N/A
Model resolution (Å)	3.7		3.9	3.9
FSC threshold	0.5		0.5	0.5
Model resolution range (Å)	3.2–4.3		3.2–7.0	3.2–7.0
Map sharpening B factor (Å^2)	−58		−130	−132
Model composition				
Non-hydrogen atoms	5333		11842	8550
Protein residues	708		1526	1113
Ligands	2		6	4
B factors (Å^2)				
Protein	50.21		66.78	64.11
Ligand	48.74		67.63	44.84
R.m.s. deviations				
Bond lengths (Å)	0.004		0.004	0.003
Bond angles (°)	0.683		0.847	0.692
Validation				
Mol Probity score	1.95		1.66	1.67
Clashscore	8.77		11.90	10.01
Poor rotamers (%)	0.00		0.00	0.00
Ramachandran plot				
Favoured (%)	92.29		97.66	97.16
Allowed (%)	7.21		2.34	2.84
Disallowed (%)	0.00		0.00	0.00

Extended Data Table 2 |

X-ray data collection and refinement statistics of *Arabidopsis* NPR1(ΔSBD) and TGA3 NID

	NPR1ΔSBD (PDB 7MK3)	**TGA3 NID (PDB 7TAE)**
Data collection		
Space group Cell dimensions	P 41 21 2	C 2 2 21
a, *b*, *c* (Å)	78.98, 78.98, 395.37	68.39, 101.74, 83.95

	NPR1ΔSBD (PDB 7MK3)	**TGA3 NID (PDB 7TAE)**
α, β, γ (°)	90.00, 90.00, 90.00	90, 90, 90
Resolution (Å)	48.62 – 3.06 (3.17 – 3.06)[*]	43.51 – 1.50 (1.55 – 1.50)
R_{merge}	0.127 (2.003)	0.04796 (1.002)
R_{pim}	0.0202 (0.2969)	0.0137 (0.2832)
$CC_{1/2}$	0.998 (0.826)	0.999 (0.947)
$I / \sigma I$	19.97 (3.14)	25.51 (3.19)
Completeness (%)	99.84 (99.96)	99.83 (99.33)
Redundancy	42.7 (45.7)	13.2 (13.1)
Refinement		
Resolution (Å)	3.06	1.50
No. reflections	24,826 (2429)	622,057 (60,581)
R_{work} / R_{free}	0.2286 / 0.2628	0.1875 / 0.2089
No. atoms	5539	1959
Protein	5472	1757
Ligand/ion	67	30
Water	0	172
B-factors	113.76	34.72
Protein	113.78	33.49
Ligand/ion	112.03	44.48
Water	N/A	45.58
R.m.s. deviations		
Bond lengths (Å)	0.002	0.006
Bond angles (°)	0.51	0.90

[*] Values in parentheses are for highest-resolution shell.

Supplementary Material

Refer to Web version on PubMed Central for supplementary material.

Acknowledgements

We thank Y. Tada for discussion on the project and Z. Yu, X. Zhao, S. Yang and R. Yan for support in cryo-EM data collection at the Janelia Research Campus. This work was supported by grants from the National Institutes of Health R01 GM115355 to P.Z., R35 GM118036 to X.D., R01 GM141223 to A.B., R01 AI148366 to Z.G., the Duke University School of Medicine Bridge Fund to P.Z., the Howard Hughes Medical Institute to X.D. and the Intramural Research Program of the National Institute of Environmental Health Sciences (NIEHS) grant ZIC ES103326 to M.J.B. X-ray fluorescence and diffraction data were collected at the Northeastern Collaborative Access Team beamline 24-ID-C, which is funded by the National Institute of General Medical Sciences (grant P30 GM124165). The Pilatus 6M detector on the 24-ID-C beamline is funded by the NIH Office of Research Infrastructure Programs (Hight-End Instrumentation grant S10 RR029205). The SAXS measurements were performed at Beamline 12-ID-B. This research used resources of the Advanced Photon Source, a US Department of Energy (DOE) Office of Science User Facility operated for the DOE Office of Science by the Argonne National Laboratory under contract DE-AC02–06CH11357. Cryo-EM data were collected using the Thermo Fisher Scientific Titan Krios transmission electron microscopes at the Janelia Research Campus and Duke University Shared Materials Instrumentation Facility (SMIF), and the Thermo Fisher Scientific Talos Arctica transmission electron microscopes at NIEHS and the University of North Carolina at Chapel Hill (UNC).

References

1. Delaney TP, Friedrich L & Ryals JA *Arabidopsis* signal transduction mutant defective in chemically and biologically induced disease resistance. Proc. Natl Acad. Sci. USA 92, 6602–6606 (1995). [PubMed: 11607555]
2. Shah J, Tsui F & Klessig DF Characterization of a salicylic acid-insensitive mutant (sai1) of Arabidopsis thaliana, identified in a selective screen utilizing the SA-inducible expression of the *tms2* gene. Mol. Plant Microbe Interact. 10, 69–78 (1997). [PubMed: 9002272]
3. Cao H, Bowling SA, Gordon AS & Dong X Characterization of an *Arabidopsis* mutant that is nonresponsive to inducers of systemic acquired resistance. Plant Cell 6, 1583–1592 (1994). [PubMed: 12244227]
4. Glazebrook J, Rogers EE & Ausubel FM Isolation of *Arabidopsis* mutants with enhanced disease susceptibility by direct screening. Genetics 143, 973–982 (1996). [PubMed: 8725243]
5. Ryals J et al. The *Arabidopsis* NIM1 protein shows homology to the mammalian transcription factor inhibitor I kappa B. Plant Cell 9, 425–439 (1997). [PubMed: 9090885]
6. Cao H, Glazebrook J, Clarke JD, Volko S & Dong X The *Arabidopsis NPR1* gene that controls systemic acquired resistance encodes a novel protein containing ankyrin repeats. Cell 88, 57–63 (1997). [PubMed: 9019406]
7. Backer R, Naidoo S & van den Berg N The NONEXPRESSOR OF PATHOGENESIS-RELATED GENES 1 (NPR1) and related family: mechanistic insights in plant disease resistance. Front. Plant Sci. 10, 102 (2019). [PubMed: 30815005]
8. Silva KJP, Mahna N, Mou Z & Folta KM NPR1 as a transgenic crop protection strategy in horticultural species. Hortic. Res. 5, 15 (2018). [PubMed: 29581883]
9. Stogios PJ, Downs GS, Jauhal JJ, Nandra SK & Prive GG Sequence and structural analysis of BTB domain proteins. Genome Biol. 6, R82 (2005). [PubMed: 16207353]
10. Stogios PJ & Prive GG The BACK domain in BTB-kelch proteins. Trends Biochem. Sci. 29, 634–637 (2004). [PubMed: 15544948]
11. Canning P et al. Structural basis for Cul3 protein assembly with the BTB-Kelch family of E3 ubiquitin ligases. J. Biol. Chem. 288, 7803–7814 (2013). [PubMed: 23349464]
12. Zhuang M et al. Structures of SPOP-substrate complexes: insights into molecular architectures of BTB-Cul3 ubiquitin ligases. Mol. Cell 36, 39–50 (2009). [PubMed: 19818708]
13. Errington WJ et al. Adaptor protein self-assembly drives the control of a cullin-RING ubiquitin ligase. Structure 20, 1141–1153 (2012). [PubMed: 22632832]
14. Gorina S & Pavletich NP Structure of the p53 tumor suppressor bound to the ankyrin and SH3 domains of 53BP2. Science 274, 1001–1005 (1996). [PubMed: 8875926]
15. Li J, Mahajan A & Tsai MD Ankyrin repeat: a unique motif mediating protein-protein interactions. Biochemistry 45, 15168–15178 (2006). [PubMed: 17176038]
16. Sedgwick SG & Smerdon SJ The ankyrin repeat: a diversity of interactions on a common structural framework. Trends Biochem. Sci. 24, 311–316 (1999). [PubMed: 10431175]
17. Wang W et al. Structural basis of salicylic acid perception by *Arabidopsis* NPR proteins. Nature 586, 311–316 (2020). [PubMed: 32788727]
18. Mou Z, Fan W & Dong X Inducers of plant systemic acquired resistance regulate NPR1 function through redox changes. Cell 113, 935–944 (2003). [PubMed: 12837250]
19. Canet JV, Dobon A, Roig A & Tornero P Structure-function analysis of npr1 alleles in *Arabidopsis* reveals a role for its paralogs in the perception of salicylic acid. Plant Cell Environ. 33, 1911–1922 (2010). [PubMed: 20561252]
20. Bombarda E, Cherradi H, Morellet N, Roques BP & Mely Y Zn^{2+} binding properties of single-point mutants of the C-terminal zinc finger of the HIV-1 nucleocapsid protein: evidence of a critical role of cysteine 49 in Zn^{2+} dissociation. Biochemistry 41, 4312–4320 (2002). [PubMed: 11914077]
21. Hol WG Effects of the alpha-helix dipole upon the functioning and structure of proteins and peptides. Adv. Biophys. 19, 133–165 (1985). [PubMed: 2424281]

22. Tada Y et al. Plant immunity requires conformational changes of NPR1 via S-nitrosylation and thioredoxins. Science 321, 952–956 (2008). [PubMed: 18635760]
23. Manohar M et al. Identification of multiple salicylic acid-binding proteins using two high throughput screens. Front. Plant Sci. 5, 777 (2014). [PubMed: 25628632]
24. Ding Y et al. Opposite roles of salicylic acid receptors NPR1 and NPR3/NPR4 in transcriptional regulation of plant immunity. Cell 173, 1454–1467 (2018). [PubMed: 29656896]
25. Waterhouse A et al. SWISS-MODEL: homology modelling of protein structures and complexes. Nucleic Acids Res. 46, W296–W303 (2018). [PubMed: 29788355]
26. Saleh A et al. Posttranslational modifications of the master transcriptional regulator NPR1 enable dynamic but tight control of plant immune responses. Cell Host Microbe 18, 169–182 (2015). [PubMed: 26269953]
27. Maier F et al. NONEXPRESSOR OF PATHOGENESIS-RELATED PROTEINS1 (NPR1) and some NPR1-related proteins are sensitive to salicylic acid. Mol. Plant Pathol. 12, 73–91 (2011). [PubMed: 21118350]
28. Hermann M et al. The *Arabidopsis* NIMIN proteins affect NPR1 differentially. Front. Plant Sci. 4, 88 (2013). [PubMed: 23630533]
29. Lebel E et al. Functional analysis of regulatory sequences controlling PR-1 gene expression in *Arabidopsis*. Plant J. 16, 223–233 (1998). [PubMed: 9839467]
30. Kachroo A & Kachroo P Fatty acid-derived signals in plant defense. Annu. Rev. Phytopathol. 47, 153–176 (2009). [PubMed: 19400642]
31. Fu ZQ & Dong X Systemic acquired resistance: turning local infection into global defense. Annu. Rev. Plant Biol. 64, 839–863 (2013). [PubMed: 23373699]
32. Wang D, Amornsiripanitch N & Dong X A genomic approach to identify regulatory nodes in the transcriptional network of systemic acquired resistance in plants. PLoS Pathog. 2, e123 (2006). [PubMed: 17096590]
33. Pape S, Thurow C & Gatz C The *Arabidopsis PR-1* promoter contains multiple integration sites for the coactivator NPR1 and the repressor SNI1. Plant Physiol. 154, 1805–1818 (2010). [PubMed: 20935179]
34. Sievers F et al. Fast, scalable generation of high-quality protein multiple sequence alignments using Clustal Omega. Mol. Syst. Biol. 7, 539 (2011). [PubMed: 21988835]
35. Mastronarde DN Automated electron microscope tomography using robust prediction of specimen movements. J. Struct. Biol. 152, 36–51 (2005). [PubMed: 16182563]
36. Scheres SH RELION: implementation of a Bayesian approach to cryo-EM structure determination. J. Struct. Biol. 180, 519–530 (2012). [PubMed: 23000701]
37. Rohou A & Grigorieff N CTFFIND4: fast and accurate defocus estimation from electron micrographs. J. Struct. Biol. 192, 216–221 (2015). [PubMed: 26278980]
38. Punjani A, Rubinstein JL, Fleet DJ & Brubaker MA cryoSPARC: algorithms for rapid unsupervised cryo-EM structure determination. Nat. Methods 14, 290–296 (2017). [PubMed: 28165473]
39. Emsley P & Cowtan K Coot: model-building tools for molecular graphics. Acta Crystallogr. D 60, 2126–2132 (2004).
40. Afonine PV et al. Real-space refinement in PHENIX for cryo-EM and crystallography. Acta Crystallogr. D 74, 531–544 (2018).
41. Bepler T et al. Positive-unlabeled convolutional neural networks for particle picking in cryo-electron micrographs. Nat. Methods 16, 1153–1160 (2019). [PubMed: 31591578]
42. Kabsch W XDS. Acta Crystallogr. D 66, 125–132 (2010). [PubMed: 20124692]
43. Bligh EG & Dyer WJ A rapid method of total lipid extraction and purification. Can. J. Biochem. Physiol. 37, 911–917 (1959). [PubMed: 13671378]
44. Li C, Tan BK, Zhao J & Guan Z In vivo and in vitro synthesis of phosphatidylglycerol by an *Escherichia coli* cardiolipin synthase. J. Biol. Chem. 291, 25144–25153 (2016). [PubMed: 27760827]
45. Spoel SH et al. Proteasome-mediated turnover of the transcription coactivator NPR1 plays dual roles in regulating plant immunity. Cell 137, 860–872 (2009). [PubMed: 19490895]

46. Zavaliev R, Mohan R, Chen T & Dong X Formation of NPR1 condensates promotes cell survival during the plant immune response. Cell 182, 1093–1108 (2020). [PubMed: 32810437]
47. Clough SJ & Bent AF Floral dip: a simplified method for *Agrobacterium*-mediated transformation of *Arabidopsis thaliana*. Plant J. 16, 735–743 (1998). [PubMed: 10069079]
48. Schindelin J et al. Fiji: an open-source platform for biological-image analysis. Nat. Methods 9, 676–682 (2012). [PubMed: 22743772]
49. Zavaliev R & Epel BL Imaging callose at plasmodesmata using aniline blue: quantitative confocal microscopy. *Methods Mol.* Biol. 1217, 105–119 (2015). [PubMed: 25287199]

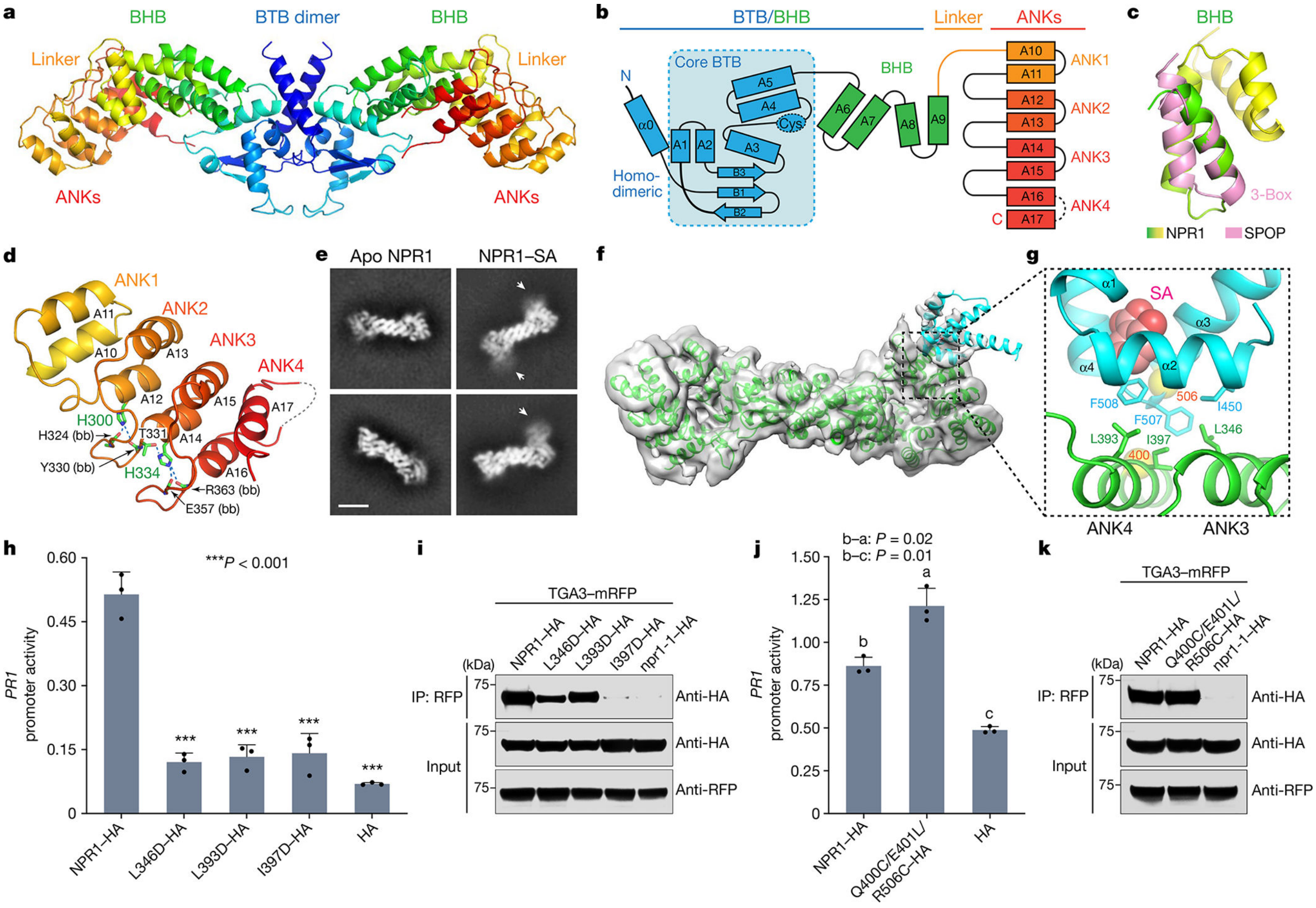

Fig. 1 |. Cryo-EM analysis of apo NPR1 and NPR1–SA.

a, The NPR1 homodimer (residues 40–402). **b**, Topology of NPR1 BTB, BHB and ANKs. Cys, cysteine cluster. **c**, Alignment of NPR1 BHB with the 3-box motif of SPOP (Protein Data Bank (PDB): 3HTM). **d**, Stabilization of NPR1 ANKs through a His300/His334-mediated hydrogen-bond network. bb, backbone amides. **e**, Representative 2D classes of NPR1 cryo-EM images without SA (left) and with SA (right). The arrows indicate the folded SBD. Scale bar, 5 nm. **f**, 3D reconstruction of full-length NPR1 showing SBD–ANK docking in the presence of SA. **g**, Hydrophobic interactions between SBD and ANK3/4. Interfacial residues (stick model), Cα atoms of Gln400 and Arg506 (yellow spheres), and SA (pink sphere model) are shown. **h**, **i**, Induction of the *PR1* promoter 24 h after SA treatment (**h**) and interaction with TGA3–mRFP (**i**) tested for HA-tagged NPR1 (NPR1–HA), npr1(L346D) (L346D–HA), npr1(L393D) (L393D–HA) and npr1(I397D) (I397D–HA). **j**, **k**, Induction of the *PR1* promoter 30 h after SA treatment (**j**) and the interactions between TGA3–mRFP and NPR1 variants (**k**), tested for NPR1–HA or npr1(Q400C/E401L/R506C) (Q400C/E401L/R506C–HA). For **h** and **j**, data are mean ± s.d. $n = 3$ independent biological replicates. P values were calculated using one-way analysis of variance (ANOVA) with Tukey's post test. The images in **i** and **k** are representatives of two biological replicates each.

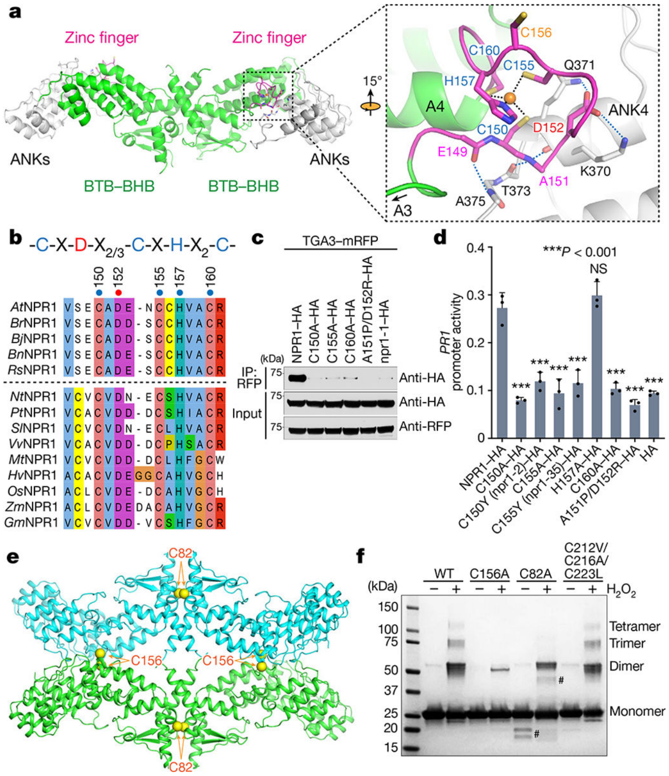

Fig. 2 |. NPR1 contains a unique zinc finger and a redox sensor.

a, NPR1 homodimer (residues 39–405) with the zinc finger detailed. The coordination of Zn^{2+} (coral sphere) by side chains of Zn^{2+}-chelating residues (shown in the stick model and labelled in blue) is indicated by black dashed lines. The hydrogen-bond network between the zinc finger and ANK4 is indicated by blue dashed lines, with the pertinent side chain and backbone groups shown in the stick model. The side chain of Cys156 is shown in the stick model. **b**, Consensus (top) and alignment showing conserved zinc finger residues (bottom) in NPR1s from different species generated by Clustal Omega[34]. Conserved residues in the consensus sequence are coloured, whereas variable residues are indicated by Xs. Proteins with and without Cys156 are separated with a dashed line. Listed plant species include: *Arabidopsis thaliana* (*At*), *Brassica rapa* (*Br*), *Brassica juncea* (*Bj*), *Brassica napus* (*Bn*),*Raphanus sativus* (*Rs*), *Nicotiana tabacum* (*Nt*), *Populus trichocarpa* (*Pt*), *Solanum lycopersicum* (*Sl*), *Vitis vinifera* (*Vv*), *Medicago truncatula* (*Mt*),*Hordeum vulgare* (*Hv*), *Oryza sativa* (*Os*), *Zea mays* (*Zm*), and *Glycine max* (*Gm*). **c**, **d**, Interaction between TGA3–mRFP and NPR1 variants (**c**) and induction of *PR1* promoter 24 h after SA treatment (**d**), tested for HA-tagged NPR1 (NPR1–HA), npr1(C150A) (C150A–HA), npr1(C150Y) (C150Y–HA), npr1(C155A) (C155A–HA), npr1(C155Y) (C155Y–HA), npr1(H157A) (H157A–HA), npr1(C160A) (C160A–HA) and npr1(A151P/D152R) (A151P/D152R–HA). For **d**, data are mean ± s.d. $n = 3$ independent biological replicates. P values were calculated using one-way ANOVA and Tukey's post test. **e**, The NPR1(ΔSBD) (Thr39–Asp410) tetramer in the protein crystal. **f**, In vitro oligomerization of NPR1 (residues Thr39–Lys262), WT or the C156A, C82A and C212V/C216A/C223L mutants, induced by hydrogen peroxide. The hash symbol (#) indicates impurity. The images in **c** and **f** are representative of two and three biological replicates, respectively.

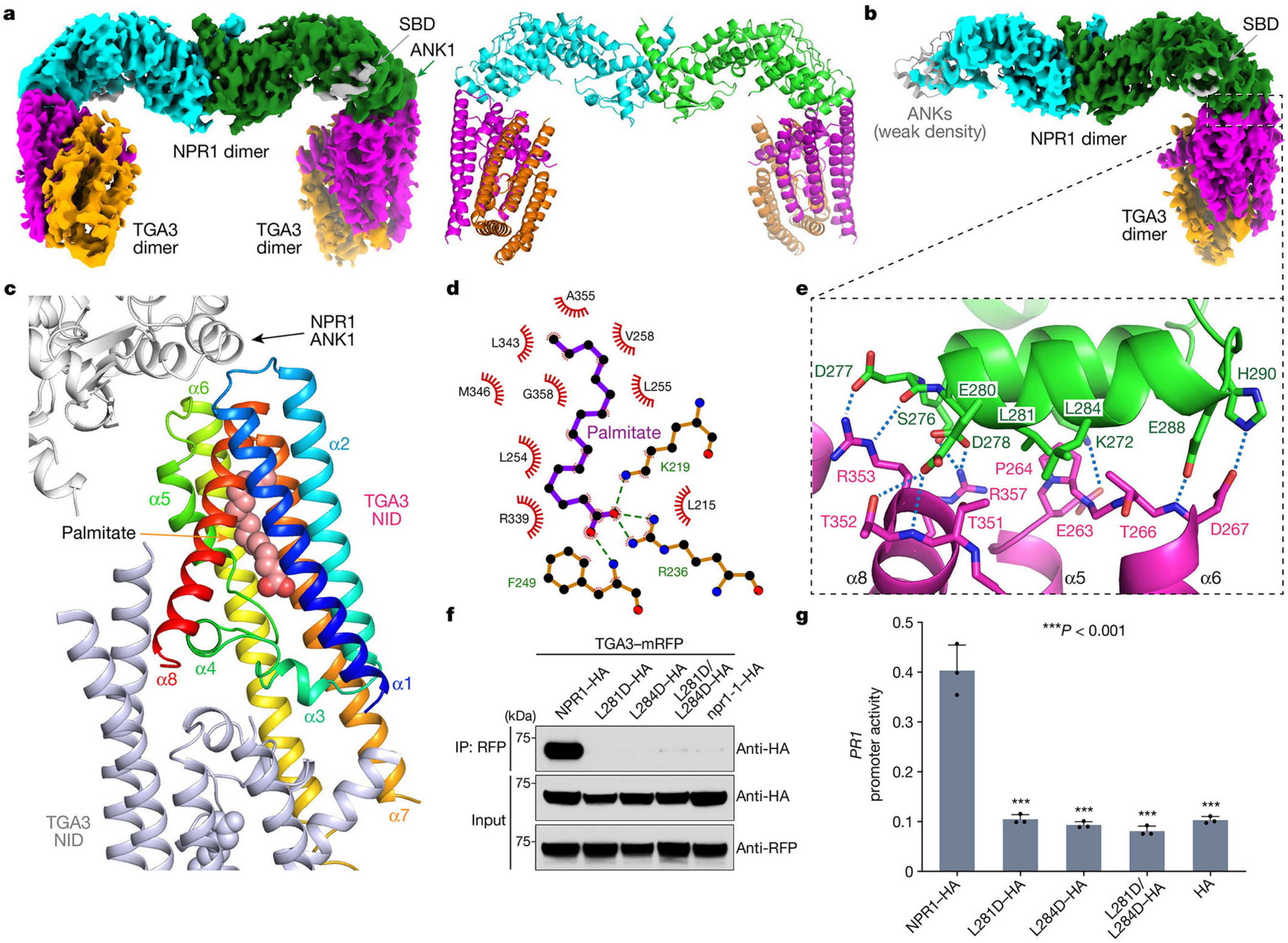

Fig. 3 |. The structure and function of the NPR1–TGA3 complexes.

a, Cryo-EM density map and cartoon representation of the TGA3_2–NPR1_2–TGA3_2 complex. **b**, Cryo-EM density map of the NPR1_2–TGA3_2 assembly intermediate. The ANK region (grey) with weak density is indicated. **c**, The palmitate-containing TGA3 NID dimer (coloured rainbow and grey). **d**, Palmitic acid recognition by the TGA3 NID in the 1.5-Å-resolution crystal structure of the TGA3 NID–palmitate complex. Polar interactions are denoted (dashed lines), and van der Waals contacts are shown (curved lines). **e**, The molecular interactions between the NPR1 ANK1 (green) and the TGA3 NID (purple). Polar interactions are indicated (dashed lines). **f**, **g**, Interactions between TGA3–mRFP and the indicated NPR1 variants (**f**) and the induction of the *PR1* promoter 24 h after SA treatment (**g**), tested for HA-tagged NPR1 (NPR1–HA), npr1(L281D) (L281D–HA), npr1(L284D) (L284D–HA) and npr1(L281D/L284D) (L281D/L284D–HA). For **g**, data are mean ± s.d. $n = 3$ independent biological replicates. P values shown were calculated using one-way ANOVA and Tukey's post test. The image in **f** is representative of two biological replicates.

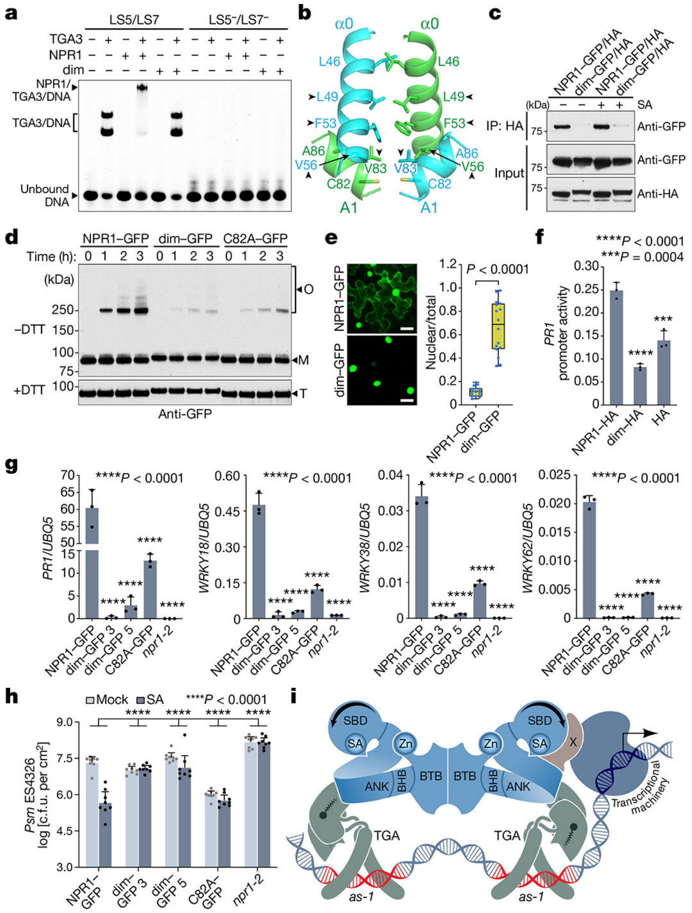

Fig. 4 |. The NPR1 dimer is required for SA-mediated immunity activation.

a, Electrophoresis mobility shift assay for TGA3 in complex with NPR1 or npr1(dim) (dim). The *PR1* promoter region with (LS5/LS7) or without (LS5⁻/LS7⁻) two *as-1* elements was used as the probe. **b**, The NPR1 dimerization interface. **c**, Self-interaction of NPR1 or npr1(dim) tested between GFP- and HA-fused proteins, with and without SA. **d**, Cell-free oligomerization of NPR1–GFP, npr1(dim)–GFP or npr1(C82A)–GFP (C82A–GFP). M, monomerized; O, oligomerized; T, total reduced proteins. **e**, Localization (left) and nucleocytoplasmic partitioning (right) of NPR1–GFP and npr1(dim)–GFP. Scale bar, 20 μm. **f**, The induction of the *PR1* promoter by NPR1–HA or npr1(dim)–HA 24 h after SA treatment. **g**, **h**, Defence gene expression (**g**) and growth of *Pseudomonas syringae* pv. maculicola (*Psm*) ES4326 (**h**) in transgenic *npr1* plants expressing NPR1–GFP, npr1(dim)–GFP lines 3 and 5, or C82A–GFP treated with 1 mM SA for 24 h. The box plot in **e** shows the median (centre line), and 25th and 75th percentiles (box limits), with the whiskers marking the minimum and maximum values. *n* = 15 (NPR1–GFP) and *n* = 16 (npr1(dim)–GFP) micrographs examined over 3 independent biological replicates. c.f.u., colony-forming units. Data are mean ± s.d. of *n* = 3 independent biological replicates (**f** and **g**); and mean ± 95% confidence intervals of *n* = 8 independent biological replicates (**h**). *P* values shown were calculated using either two-tailed Student's *t*-tests (**e**), or one-way ANOVA (**f** and **g**) and two-way ANOVA (**h**) followed by Tukey's post test. The experiments in **c**–**h** were repeated at least twice with similar results. **i**, The enhanceosome model of dimeric

NPR1 bridging two dimeric TGA transcription factors. SA-induced SBD–ANK docking creates a new interface to facilitate post-translational modifications and/or to facilitate the recruitment of transcriptional regulators (X) for the activation of defence genes. The images are representative of three (**a**, **c** and **e**) and four (**d**) biological replicates.